Characterizing the global ocean ambient noise as recorded by the dense seismo-acoustic Kazakh network

Alexandr Smirnov[1,2], Marine De Carlo[3], Alexis Le Pichon[3], Nikolai M. Shapiro[2,4,5], Sergey Kulichkov[6]

[1]Institute of Geophysical Research, Almaty, 050020, Kazakhstan
[2]Institut de Physique du Globe de Paris, Sorbonne Paris Cité, F-75005 Paris, France
[3]CEA, DAM, DIF, F-91297 Arpajon, France
[4]Institut de Sciences de la Terre, Université Grenoble Alpes, CNRS (UMR5275), Grenoble, France.
[5]Schmidt Institute of Physics of the Earth, Russian Academy of Sciences, Moscow, Russia
[6]A.M. Obukhov Institute of Atmospheric Physics RAS, Moscow, 119017, Russia

Correspondence to: Alexandr Smirnov (smirnov@ipgp.fr)

Abstract. The dense seismo-acoustic network of the Institute of Geophysical Research (IGR), National Nuclear Center of the Republic of Kazakhstan, has been operating in Kazakhstan since the late nineties of the last century. It consists of five seismic and three infrasonic arrays. The IGR network includes stations that are part of several national and global monitoring systems. Infrasonic and seismic data are processed using the Progressive Multi-Channel Correlation (PMCC) detector to characterize the temporal variability of microbarom and microseism signals from 2014 to 2017. The non-linear interaction of ocean waves is simulated using the microseism source model distributed by the French Research Institute for Exploitation of the Sea (IFREMER). The wave attenuation is calculated using a semi-empirical propagation law in a range independent atmosphere. The observed and predicted infrasonic and seismic signals are compared, confirming a common source mechanism for both microbaroms and microseisms. This study reveals the dominating directions of arrivals at each station of the IGR network and the associated source regions. Multi-year and intra-seasonal parameter variations are analysed, revealing the strong influence of long-range atmospheric propagation on microbarom predictions. In winter, dominating sources of microbaroms are mainly located in the North Atlantic and in the North Pacific during Sudden Stratospheric Warming (SSW) events while signals observed in summer likely originate from source regions in the southern hemisphere.

Introduction

Pressure fluctuations of ocean infra-gravity gravity waves are primarily at the origin of seismic ambient noise categorized as seismic hum (1–20 mHz), primary microseisms (0.02–0.1 Hz), and secondary microseisms (0.1-1 Hz). The theory to predict

microseisms and microbarom source regions was developed by Longuett-Higgins (1950). This theory explains how counter propagating ocean waves can generate propagating acoustic waves and create secondary microseisms by exciting the sea floor. Gutenberg (1953) first pointed out the relation between microseisms, meteorological conditions, ocean waves, and microbaroms. Hasselmann (Hasselmann, 1963, 1966) generalized Longuett-Higgins' theory to random waves by investigating

35 non-linear forcing of acoustic waves. Donn and Naini (1973) suggested a common source mechanism of microbaroms and microseisms from the same ocean storms demonstrating that the only mechanism capable of transmitting energy into both the atmosphere and the sea bottom is associated with the surface waves in a storm area. Microseism modelling was introduced by Kedar et al. (2008). The good correlation between the observed microseism amplitudes and their predicted values according to the Longuett-Higgins theory was shown, demonstrating that microseism source locations can be tracked using numerical

40 modeling (Shapiro, 2005; Shapiro and Campillo, 2004; Stehly et al., 2006; Stutzmann et al., 2012; Weaver, 2005).

A radiation model of microbaroms from the motion of the air/water interface was later proposed by Waxler and Gilbert (2006). Ardhuin and Herbers (Ardhuin and Herbers, 2013a) developed a numerical model based on Longuett-Higgins-Hasselmann theory for the generation of Rayleigh waves, considering an equivalent pressure source at the undisturbed ocean surface. The different patterns between microseismic body and surface waves resulting from distinctive amplification of ocean wave-

45 induced pressure perturbation and different seismic attenuation have been studied with implications for seismic imaging and climate studies (Obrebski et al., 2013). Coastal reflections also play an important role in the generation of microbaroms and microseisms but modelling the reflection of ocean waves off the coast still remains a major source of model uncertainty (Ardhuin et al., 2013b).

As for microseisms, microbaroms are not the impulsive signals but quasi-monochromatic sequences of permanent waves

50 (Olson and Szuberla, 2005); therefore, it is not possible to detect their onset and identify their propagation paths. However, these signals are well detected using standard processing techniques, such as beamforming methods used from the sixties (Capon, 1972; Haubrich and McCamy, 1969; Toksoz and Lacoss, 1968). Several studies demonstrated the efficiency of beamforming approaches (e.g. Evers and Haak, 2001) or correlation-based methods (e.g. Garcès, 2004; Landès et al., 2012) to detect and characterize microbarom signals globally.

55 The microbarom frequency band is at the lower edge of the frequency band of interest to monitor nuclear tests. Recent global scale microbarom observations recorded by the International Monitoring System (IMS) network of the Comprehensive Nuclear Test Ban Treaty Organization (CTBTO) confirm that its detection capability is highly variable in space and time (Ceranna et al., 2019). Thus, in order to assess the microbarom source intensity accurately, it is necessary to take into account a realistic description of the middle atmosphere. Other studies have been conducted to characterize the ambient infrasound noise. Smets

60 et al. (2014) compared three months of microbarom observations with the expected values to study the life cycle of Sudden Stratospheric Warming events. Landès et al. (2014) compared the modelled source region with microbarom observations at operational IMS stations. Le Pichon et al. (2015) compared observations and modelling over a 7-month period to assess middle atmospheric wind and temperature models distributed by European Centre for Medium-Range Weather Forecasts (ECMWF).

More recently, Hupe at al. (2018) showed a first order agreement between the modelled and observed microbarom back-azimuth and amplitude in the Northern Atlantic.

In this paper, we further extend the approach developed by Hupe at al. (2018) by densifying the monitoring network. The considered dense seismo-acoustic Kazakhstani network is operated by the Institute of Geophysical Research (IGR) of the National Nuclear Center of the Republic of Kazakhstan and includes both seismic and infrasound arrays. Using such experimental setting, we aim at developing synergetic approaches to better constrain microbarom source and evaluate propagation effects. Since the pioneer work of Donn and Naini (1973), this study is to our knowledge the first multi-year comparisons between observed and modelled microbaroms and microseisms at co-located seismo-acoustic arrays. In the first part, we present the observation network and methods used in this study. In the second part, the processing and modelling results of microseism and microbarom signals recorded by the IGR seismo-acoustic network from 2014 to 2017. In the last part, comparisons between microbarom predictions and observed microbaroms and microseisms signals are discussed.

1 Observation network and methods

1.1 Observation network

The Kazakhstani seismo-acoustic network (KNDC, 2019) is unique for microbarom and microseism studies, as it contains five seismic and three infrasound arrays (Figure 1).

The infrasound network consists of the IMS infrasound station IS31 located in north-west Kazakhstan (2.1 km aperture, 8 elements), two national arrays of 1 km aperture: KURIS (4 elements) near the Kurchatov and MKIAR (9 elements) near the Makanchi village (Belyashov et al., 2013) (Figure 1). KURIS and MKIAR have been operating since 2010 and 2016, respectively. Microbarometers MB2000 and MB2005 are used at IS31 and KURIS, and Chaparral Physics Model 25 microbarometers are installed at MKIAR. Figure 2 shows the frequency response of the microbarometers. These stations form a unique dense regional infrasound network. Combining infrasound observables recorded by this network allows discriminating between regional natural and anthropogenic sources (Smirnov, 2015; Smirnov et al., 2011, 2018).

The seismic network consists of Kurchatov Cross array and MKAR part of the IMS network, ABKAR and KKAR part of the Air Force Technical Applications Center (AFTAC, USA) network (Figure 1 and Table 1). The Kurchatov cross array consists of 20 elements arranged in a cross with an aperture of 22 km (Figure 1). It consists of Guralp CMG-3V sensors. While in the 0.1-0.3 Hz band, MKAR, ABKAR, and KKAR sensors are at out of the frequency band of interest (0.1-0.3 Hz), the frequency response of the Kurchatov cross array is flat within the secondary microseismic band. The configuration of ABKAR, BVAR, KKAR and MKAR are similar with nine elements and an aperture of ~5 km. The ABKAR array configuration is shown as callouts in Figure 1. These arrays are equipped with Geotech Instruments GS21 short period vertical sensors with a flat response for frequencies above 1 Hz. Figure 3 shows the frequency response of GS-21 and CMG-3V sensors within the frequency range of 0.1-0.4 Hz. Surface waves from the ocean storms are well recorded by broad band seismometers. Body

waves are also registered on GS21 short period sensors. Although, in the frequency band of interest the signal attenuation is about 30 dB, all stations detect microseisms effectively due to their large amplitude above the background noise. A peculiarity of the network is that infrasound and seismic arrays are collocated at two sites (KURIS and Kurchatov Cross; MKIAR and MKAR) or installed relatively close to each other (IS31 and ABKAR are 220 km apart, Figure 1). Figure 4 and Figure 5 show typical power spectral density (PSD) of the ambient noise for the infrasound and seismic arrays, respectively. The PSD calculation was carried out using one-hour time window during calm periods on October 23 and July 15. The microbarom peak clearly appears at all infrasound arrays only in October. In the summertime, this peak is visible only at IS31. As opposed to the infrasound noise, the seismic noise spectra exhibit the microseismic peak in both seasons with an overall noise level in October approximately 10 dB higher than in July. This effect is most pronounced at the Kurchatov Cross array.

1.2 Processing method

Microseisms are detected using the Progressive Multichannel Correlation Method (PMCC) (Cansi, 1995; Cansi and Klinger, 1997; Smirnov et al., 2011) in 10 linearly spaced frequency bands between 0.05 and 0.4 Hz. A fixed time window length of 200 s is used for each sub-band. For infrasound processing, the frequency band is broadened to 0.01-4 Hz using fifteen logarithmically scaled sub-bands, and time window length varying from 30 s to 200 s (Matoza et al., 2013). Only detections with a mean frequency ranging in the 0.1–0.4 Hz microbarom band are considered.

It is important to take into account uncertainties in azimuth and apparent velocity estimations identified in microbarom studies. The uncertainties of the estimated wave parameters of microseisms can be large due to the relatively small aperture of the seismic arrays. Uncertainties in wave parameter estimates are calculated considering the array geometry of the above mentioned infrasound and seismic arrays (Szuberla and Olson, 2004) (Table 1). For the infrasound arrays, the horizontal velocity is set to 340 m/s. For the seismic arrays, the value of 3000 m/s is chosen corresponding to the average speed of the Rayleigh wave. The uncertainties for the seismic arrays are significantly higher for the body waves due to higher velocities. It should be noted that these errors are optimistic as the estimation do not take into account site and time dependent signal-to-noise ratio.

1.3 Source modelling

Sources of microseisms are distributed by IFREMER (IFREMER, 2018) referred to as 'p2l' – as a composite calculated from the wave-action WaveWatch III model (WW3) developed by the National Oceanic and Atmospheric Administration (NOAA). While the bathymetry strongly affects the source intensity in microseism modelling (Ardhuin et al., 2011; Ardhuin and Herbers, 2013a; Kedar et al., 2008), a recently modeling study by De Carlo (2020) suggests that bathymetry has negligible impact on microbarom source strength in contrast to predictions from the model by Waxler (2007). In this study, the source term at the ocean surface for microseisms ('p2l') which does not include coupling with the bathymetry is taken as a proxy to model microbaroms). To model microbarom signals, the WW3 wave action model developed by NOAA and distributed by

IFREMER was used. While microseisms propagate through the static structure of the solid Earth, , microbaroms are primarily affected by the strong spatio-temporal variability of the temperature and wind structure of the atmosphere. Therefore, the geometrical spreading and seismic attenuation are the main effects to account for microseism modelling (e.g. Kanamori and Given, 1981; Stutzmann et al., 2012), while the dynamical properties of the middle atmosphere should be taken into account for microbarom modelling.

1.3.1 Source modeling for microbaroms

Microbarom sources are computed following the approach developed by De Carlo et al. (2018, 2020). Simulations are carried out using the microbarom generation theory at the microseismic secondary peak (0.1-1 Hz) based on the non-linear oceanic wave interaction (Ardhuin and Herbers, 2013a). Input data are calculated over a global grid of resolution 0.5° in space and 6 hours in time. For the attenuation, we use a semi-empirical frequency dependent attenuation relation derived from massive parabolic equation simulations and consider realistic propagation scenarios. Atmospheric specifications are given by the high-resolution forecast (HRES) that is part of ECMWF's Integrated Forecast System (IFS) cycle 38r2 (Le Pichon et al., 2012). Atmospheric profiles are given at the station and are assumed to be constant along the propagation path. This approach shows overall first order agreement between microbarom observations and predictions generated in the northern hemisphere similar to those described by De Carlo et al. (2018) and Hupe et al. (2018) (in a range of ~10° for the back-azimuths).

The correlation coefficient between the observed and predicted seasonal patterns is calculated following metrics elaborated by Landès (Landès et al., 2014). There are two different metrics: (i) S_{corr_Az} which defines the correlation between the observed (N_{obs}) and predicted (N_{pred}) marginal detection number in the direction θ_{Amax} versus time (t):

$$S_{corr\_Az} = C_{corr} [N_{obs} (\theta_{Amax}, t), N_{pred} (\theta_{Amax}, t)] \tag{1}$$

and (ii) S_{corr_Amp} for the correlation between the predicted and observed amplitude A_{max}.

$$S_{corr\_Amp} = C_{corr} [N_{obs} (A_{max}, t), N_{pred} (A_{max}, t)] \tag{2}$$

Figure 6 shows the distribution of the epicenters of the expected microbarom sources from January to February 2017. The map shows regions of the globe from where signals recorded at IS31 with the largest amplitude originate. The calculation was carried out for two winter and two summer months. The distribution of the epicenters is not uniform, appearing as several aggregations shown on the maps as coloured surfaces according to the dominant frequencies of the predicted sources and expected amplitudes at the station. The digits on the map indicate the mean amplitude and frequency of the corresponding clusters.

1.3.2 Source modeling for microseisms

The bathymetry effect plays an important role when calculating the microseism source intensity. Longuet-Higgins (1950) showed that the pressure fluctuations do not attenuated with depth but are transmitted to the ocean bottom as acoustic waves.

Depending on the ratio between the wavelength of the acoustic waves and the ocean depth, resonance effects can occur leading to a modulation of the pressure fluctuations at the sea floor (Stutzmann et al., 2012). The corresponding seismic source power spectral density at the ocean bottom is:

$$S_{DF}(f_s = f_2) = \frac{2\pi f_s}{\rho_s^2 \beta^5} \left[\sum_{m=1}^{m=N} c_m^2\right] F_p(\mathbf{K} \cong 0, f_2 = 2f) \tag{3}$$

160   Equation (3) is derived from Longuet-Higgins equation (186). S_{DF} is in m/Hz. ρ_s and β are respectively the density and S-wave velocity in the crust. f_s is the seismic frequency which is equal to the pressure fluctuation frequency f_2 and it is the double of the ocean wave frequency f. Coefficients c_m correspond to the compressible ocean amplification factor. c_m are non-dimensional numbers which vary between 0 and 1 as a function of the ratio $2\pi f 2h/\beta$ where h is the water depth (Longuet-Higgins, 1950). Considering the crustal density $\rho_s = 2600$ kg m^{-3} and S-wave velocity $\beta = 2800$ m/s, Figure 7 shows the map of the sources of

165   microseism distribution for ABKAR.

2 Results

2.1 Processing results

Signals from the ocean storms are successfully extracted from the records at all IGR infrasound and seismic arrays. Diagrams in this section show the back-azimuths of the signals as a function on time. Distributions of the maximum amplitudes are

170   included as well. The amplitude maxima are found in the PMCC bulletins each 6 hours of the entire period of 2014-2017.

2.1.1 Microbaroms

Signals from ocean storms recorded at infrasound and seismic arrays are successfully identified. Figure 8 to 10 show the temporal variation of the dominant microbarom signals for infrasound arrays IS31, KURIS and MKIAR, respectively. The amplitudes and back-azimuths of the dominant microbarom signals are selected from the PMCC bulletins and are plotted as

175   orange dots.

The graphs show pronounced seasonal variations for both back-azimuths and amplitudes. The largest amplitudes are observed by IS31 during the winter months, when signals with back-azimuths of 320±20° prevail (Figure 8). Few detections with back-azimuths of 35±15° are also detected in winter. During the summer months, low-frequency signals with back-azimuths of 210±50° dominate. In winter, the amplitudes range from ~0.001 to ~0.1 Pa, the largest values being observed in winter.

180   Figure 9 shows the observational data for KURIS. The back-azimuths measured at this station are similar to those recorded at IS31, with slightly higher values in winter (325±15°). In summer, two regimes are distinguished in the azimuthal ranges of 230±30° and 130±30°. Detections near 50° are also observed in winter. Similarly to IS31 data, KURIS data shows that maximum microbarom amplitudes are observed in winter. From summer to winter, the maximal signal amplitude increases from 0.001 to 0.03 Pa.

185   MKIAR started recording microbaroms in August 2016 with repetitive seasonal variations (Figure 10). One cluster of detections dominates in winter at ~330°and two clusters in summer at 230° and 110° with a corresponding standard deviation of ±10°, 25° and 25°, respectively.

2.1.2 Microseisms

Figure 11 shows results for ABKAR seismic array. In addition to the observations, the diagrams represent the simulated
190 microseism parameters. Amplitudes are the largest in winter where detections with back-azimuths of 340±20° prevail. During summer months, signals with back-azimuths of 290±20° dominate. The amplitudes range from ~0.4 to ~20 nm/s varying from the largest values in winter to minimum values in summer. Figure 12 shows results for KKAR. Two clusters of detections at 330±20° and 5±5° is observed in winter while in summer there are clusters at 160±20° and 190±15°. The seasonal amplitude variation is 0.5-7.0 nm/s. Figure 13 shows the results for Kurchatov Cross. In winter, back-azimuths of microseisms are
195 300±20°. A small amount of signals with 50±50° is observed in summer. Amplitudes reach their maximum in winter and minimum in summer, ranging from 8 to 200 nm/s. This is significantly higher than for all other arrays because Kurchatov Cross array is equipped with broad-band seismometers while all the other arrays register signals with short period sensors, showing amplitude frequency response falloff within the surveyed frequency range. Figure 14 shows results for MKAR. Two clusters at 310±20° and 5±5° are observed in winter while in summer there are clusters at 130±10° and 180±10°. The seasonal
200 amplitude variation is 0.7-7.3 nm/s. The seasonal trend of the maximum microseism amplitudes recorded at all seismic stations is similar, with a maximum observed in winter. At MKAR and KKAR, microseism amplitudes are characterized by a slight increase in the middle of summer which could be related with the southern location of these arrays. Such a peak is not observed at ABKAR. At the Kurchatov Cross station, there are a small amount of detections in summer which could be explained by higher noise level or a loss of signal coherency at this site. The graphs clearly show that the amplitudes vary synchronously
205 even at smaller time scale (Figure 17). However, a decrease in amplitude is observed early January 2017 at all stations. As expected, the maximum amplitudes in winter decrease with increasing distance from the stations to the North Atlantic region (about 10, 8, and 4 nm/s for ABKAR, KKAR, and MKAR, respectively). At Kurchatov, the amplitude is significantly higher in winter (in the order of 80 nm/s).

2.2 Modelling results

210 The back-azimuths and amplitudes have been calculated for the expected microbarom sources at IS31, KURIS, and MKIAR. The expected distances to the source regions vary with season. For example at IS31, simulations predict in winter three source regions (Figure 6 a); distances to North Atlantic regions range between 3500 to 7000 km while the distance to the North Pacific region is around 7000 km. In summer, additional microbarom sources are located in the southern hemisphere at distances larger than 11000 km (Figure 6 b). Figure 8 to 10 compare the observed and predicted arrivals at these stations. During winter
215 months, a good agreement is found: IS31 records microbaroms with back-azimuths of 320±20° within the predicted range (Figure 8 a and c). A good agreement is also observed at KURIS (Figure 9 a, c) and MKIAR (Figure 10 a, c). During the

summer months, the agreement in azimuths remains satisfactory at all stations within a range of ±30°. IS31 records microbaroms within 210±50° with a slight shift compared with the predicted system (185±50°). At KURIS, the observed systems 230±30° and 130±30° are different compared with the predicted ones (±10° and 160±10°). At MKIAR, during the summer months, microbaroms within the predicted range of 60-270° are consistent with the observed systems (230±25° and 110±25°). As the used source model was developed for microseisms (Ardhuin et al., 2011), an empirical scaling factor (F = 1:10000) has been applied to account for wave coupling effect in the atmosphere, thus allowing qualitative comparisons between the observed and predicted temporal variations of the microbarom amplitudes. At all stations, there is good agreement between the predicted and observed amplitudes during the winter months (Figure 8 d, Figure 9 d and Figure 10 d), but in summer the predicted amplitudes are overestimated when compared to the observed ones (Table 2).

To summarize, both amplitudes and azimuths are well predicted in winter as opposed to summer months. The observed discrepancies are explained here by unrealistic simulated wave attenuation for dominating sources located in the southern hemisphere due to the assumed range independent atmosphere. Quantitative estimations of the prediction quality (S_{corr} calculated according to equations (1) and (2)) are summarized in Table 2.

3 Discussions

Where previous studies analysed microbarom signals at a single station (Hupe et al., 2018), further investigations are conducted in this study by considering a multi-year dataset of continuous records collected by the IGR network. Regional features of both microbaroms and microseisms are highlighted.

Figure 15 shows the azimuthal distribution of infrasound detections having maximum amplitudes. The histograms of the azimuthal distribution of microbaroms clearly show the dominating direction of arrivals in winter with prevailing directions ranging from 270 to 350° (Figure 15 b). The predicted azimuths are in good agreement with the observed ones (Figure 8 c, Figure 9 c, Figure 10 c, Figure 15 b and Table 2). Observations, as well as simulations, show large temporal variations in the dominating microbarom source regions explained by the seasonal reversals of the prevailing stratospheric winds, which in turn, cause the migration of storm activity area to the winter hemisphere (Stutzmann et al., 2012).

Figure 16 shows similar histograms for seismic stations. One can distinguish seasonal trends for both infrasonic and seismic observations. In winter, microbaroms and microseisms are detected from northern and north-western directions (Figure 15 b and Figure 16 b). In summer, southern, southwestern and south-eastern directions dominate (Figure 15 c and Figure 16 c). Signals from north-western direction are also recorded at ABKAR, KKAR, and MKAR in summer. Azimuths differ from one station to another depending on the strongest microbarom and microseism source regions relative to the station locations. As for microbaroms, during winter months, microseism observations exhibit a similar pattern with a larger spreading (250-360°), and an additional peak (0-20°) at KKAR and MKAR (Figure 16). These peaks are explained by body and seismic surface waves. In winter, microseisms exhibit similar trends with some difference as shown by Figure 11 c, Figure 12 c, Figure 13 c, Figure 14 c and Figure 16 b. The dominant directions are comparable with a larger spreading: from 250° to 360° and from 0°

to 20°. For KKAR and MKAR, two peaks are seen in the histograms, with a second peak at 0-20°. These peaks could likely be explained by body and surface seismic phases identified by high trace velocity values. Microbaroms are predicted mainly from the southern direction (180-200°). Such a peak is observed only at IS31 and MKAR (Figure 15 c). The closest peak observed at KURIS and MKIAR is shifted northwards by ~50°. The dominant back-azimuths are close to 90°. At MKIAR the peak is around 100°.

Thus, in winter, signals from ocean storms in the North Atlantic region dominate at all stations. This is supported by the microbarom and microseism simulation results which account for the predicted source regions, bathymetry, and propagation effects. More complicated picture is observed at summer months. Some stations detect signals from regions along the peri-Antarctic belt while simulations predict microbaroms with larger amplitude summer. Other stations detect signals from the south, but the detected back-azimuths disagree with the predictions.

Using historical IGR datasets, the spatiotemporal variability of microbarom signals due to changes in the source location and the structure of the atmospheric waveguides can be studied. There is a clear seasonal trend in the directions and amplitudes of microbaroms and microseisms (Figure 8, Figure 9 and Figure 10). Moreover, microseism amplitudes synchronously vary at all stations (Figure 17). A similar pattern is shown for microbaroms (Figure 18). A better agreement between observations and simulations is found for the azimuths.

As already shown by Evers and Siegmund (2009) and Smets and Evers (Smets and Evers, 2014), the life cycle of Sudden Stratospheric Warming (SSW) events can be inferred from the observed spatio-temporal variations of microbarom parameters. Such observations are noted at IS31 where microbaroms in early and late February 2017 shifted to easterly directions (~40°) consistent with the simulated source regions in the Northern Pacific (Figure 8). As noted for IS31, KURIS also recorded signals with back-azimuths of ~40° in late January 2017 (Figure 9). Similarly, signals from ~100° were also recorded during the 2017 SSW event at MKIAR. However, the observed back-azimuths differ from those expected (~60°). It is likely that this station recorded signals from other regions over the Pacific Ocean which are not described by the ocean wave model.

These findings are consistent with comparisons between the observed and modelled microbarom signals carried out by Landès et al. (2014) at IS31. This study shows that modelling well describes microbarom sources in the North Atlantic in winter and poorly explains signals in summer.

Comparison between seismic and infrasound bulletins at collocated sites highlight comment features. Figure 19 presents the observed back-azimuths and signal amplitudes from 1 January 2014 to 31 December 2017 at ABKAR and IS31arrays located 230 km apart. Figure 20 shows the detections results for the collocated Kurchatov Cross and KURIS arrays. . The comparison of the bulletins in Figure 19, and Figure 20 shows similar seasonal patterns:.

- North Atlantic microseisms and microbaroms prevail in array records in winter months. Back-azimuths of approximately 300-360° are clearly visible in Figure 19 a,b, and Figure 20 a, b.

- Amplitudes of North Atlantic microbaroms and microseisms exceed large amplitude during summer months as shown by Figure 19 c,d, Figure 20 c,d.

At the same time, specific features are identified:

- Arrays record North Atlantic microseisms more steadily than microbaroms from that region. Figure 19 a,b, Figure 20,b clearly show that microseisms dominate microbaroms.

285
- The range of back-azimuths for North Atlantic microseisms is larger than the ones of microbaroms for ABKAR and MKAR (Figure 19 a,b, and Figure 20,b).

- For all infrasound arrays, back-azimuths of North Atlantic microbaroms are larger (320-330°) (Figure 19 b and Figure 20 b). Back-azimuths differ from one seismic array to another: 330-350° for ABKAR array (Figure 19a), 290-310° for Kurchatov Cross array (Figure 20 a) and 310-320°.

290
- In summer months, no correlation is found in the prevailing directions of microseism and microbarom arrivals for collocated arrays (Figure 19 a and b, Figure 20 a,b)

This study provides a first characterization of the seasonal patterns of microbarom and microseisms recorded by the IGR seismo-acoustic network. The chosen detection algorithm and propagation model offer a good trade-off between low calculation effort and propagation accuracy. Identified shortcoming is the limitation of PMCC to detect overlapping
295 microbarom sources originating from different directions. Furthermore, the approach assuming range-independent atmosphere may lead to erroneous interpretations for situations involving long propagation ranges where significant along-path variability of wind and temperature profiles may occur, in particular when modeling the relative strength of microbarom sources located in different hemispheres.

Conclusions

300 The IGR seismo-acoustic network is much denser than the global IMS infrasound network. Analyzing multi-year archives of continuous recordings provides a detailed picture of the spatial and temporal variability of the seismic and infrasound ambient noise originating from two hemispheres. In winter, the most intense oceanic storms are modelled in the Northern Atlantic and their signature prevails on infrasound and seismic records. During minor SSWs, bi-directional conditions may occur which may have strong impacts on the retrieved microbarom signals (Assink et al., 2014). Simulated and observed microbarom
305 parameters are consistent, as shown by high correlation coefficients. The largest amplitudes of both microbaroms and microseisms are found for sources in the Northern Atlantic. Exploiting the synergy between seismic and infrasound ambient noise observations is thus valuable to: (i) better constrain the source strength using seismic records as microseisms propagation through the static structure of the Earth, (ii) improve the detectability of ocean-wave interaction and location accuracy as microbarom wave parameters are less affected by heterogeneities in the propagation medium, and (iii) improve the physical
310 description of seismo-acoustic energy partitioning at the ocean-atmosphere interface.

Further numerical investigations are needed to define the most suitable detection parameters in terms of missed events and false alarm rate, and estimate wave parameter uncertainties accounting for the response functions of all arrays. In this study, part of the discrepancies between observations and predictions motivate the use of high-resolution detection methods to identify multiple propagation paths from which microbarom energy can reach the array (e.g., Assink et al., 2014). Exploring the capability of high-resolution detection processing techniques to extract multidirectional overlapping coherent energy would be valuable to provide a more realistic picture of the recorded ocean ambient noise (e.g., den Ouden et al., 2020).

Additional studies are required to further evaluate whether the bathymetry effect could explain discrepancies between the observed microbarom and microseism signals (Longuet-Higgins, 1950; Stutzmann et al., 2012, De Carlo 2020). In summer, the microbarom and microseism sources which dominate in the southern hemisphere more especially along the peri-antarctic belt are likely at the origin of the weak signals observed south of the IGR network. For such long propagation ranges, more realistic numerical simulations could reduce the differences between the observed and modelled amplitude; additional studies are thus required to explore time- and range-dependent full-wave propagation techniques while still maintaining computational efficiency (e.g., Waxler and Assink, 2019). Including additional data from other seismo-acoustic network in the southern hemisphere would help validating long-range propagation modelling, better characterize station-specific ambient noise signatures, and enhance discrimination methods at a regional scale.

Code/Data availability

Atmospheric wind and temperature profiles are derived from operational high-resolution atmospheric model analysis, defined by the Integrated Forecast System of the ECMWF, available at https://www.ecmwf.int/ (last access: 2 September 2019; ECMWF, 2018). Waveform data for the seismic and infrasound arrays of the CTBTO IMS (https://www.ctbto.org/, last access: 2 September 2019) used in this study are available to the authors, being members of National Data Centers for the CTBTO. Data of the Kazakhstani national seismic and infrasound arrays are available under request from the Institute of Geophysical Researches, National Nuclear Center of Kazakhstan. Results of the microseism and microbarom detections by the seismo-acoustic Kazakh network and of the microbarom simulation for the infrasound arrays of the network are available at ISC repository (Smirnov et al., 2020).

Author contribution

N. Shapiro and A. Le Pichon suggested main outlines of the paper. A. Smirnov and A. Le Pichon prepared historical dataset for processing. M. De Carlo and A. Le Pichon developed the microbarom source model. A. Smirnov performed microbarom and microseism detections and propagation simulations. A. Smirnov prepared the manuscript with contributions from all co-authors. A. Le Pichon, M. De Carlo and S. Kulichkov made critical reviews and comments to improve the manuscript.

Competing interests

The authors declare that they have no conflict of interest.

Acknowledgements

This research has been supported by the Commissariat à l'Energie Atomique (CEA, France). The work of NS has been

345   supported by the European Research Council (ERC) under the European Union Horizon 2020 Research and Innovation Programme (grant agreement 787399-SEISMAZE), the Russian Ministry of Education and Science (grant N 14.W03.31.0033) and Russian Foundation for Basic Research (project no. 18-05-00576). Authors also thank Anna Smirnova for the help in the manuscript preparation.

References

350

Ardhuin, F., Stutzmann, E., Schimmel, M. and Mangeney, A.: Ocean wave sources of seismic noise, J. Geophys. Res., 116(C9), doi:10.1029/2011jc006952, 2011.Ardhuin, F. and Herbers, T. H. C.: Noise generation in the solid Earth, oceans and atmosphere, from nonlinear interacting surface gravity waves in finite depth, J. Fluid Mech., 716, 316–348, doi:10.1017/jfm.2012.548, 2013a.

355 Ardhuin, F., Lavanant, T., Obrebski, M.: A numerical model for ocean ultra-low frequency noise: wave-generated acoustic-gravity and Rayleigh modes, J. Acoust. Soc. Am., 134, doi:10.1121/1.4818840, 2013b.

Assink, J. D., Waxler, R., Smets, P. and Evers, L. G.: Bidirectional infrasonic ducts associated with sudden stratospheric warming events, J. Geophys. Res. Atmos., 119(3), 1140–1153, doi:10.1002/2013jd021062, 2014.

Belyashov, A., Dontsov, V., Dubrovin, V., Kunakov, V. and Smirnov, A.: New infrasound array "Kurchatov", NNC RK Bull.,
360 (2), 24–30, 2013.

Cansi, Y.: An automatic seismic event processing for detection and location: The P.M.C.C. Method, Geophys. Res. Lett., 22(9), 1021–1024, doi:10.1029/95gl00468, 1995.

Cansi, Y. and Klinger, Y.: An Automated Data Processing Method for Mini-Arrays, Newsl. Eur. Seismol. Cent., 1021–1024, 1997.

365 Capon, J.: Long-Period Signal Processing Results for LASA, NORSAR and ALPA, Geophys. J. Int., 31(1–3), 279–296, doi:10.1111/j.1365-246x.1972.tb02370.x, 1972.

De Carlo, M., Le Pichon, A., Ardhuin, F. and Näsholm, S.: Characterizing and modelling ocean ambient noise using infrasound network and middle atmospheric models, NNC RK Bull., (2), 144–151, 2018.

De Carlo, M., Ardhuin, F., and Le Pichon, A.: Atmospheric infrasound generation by ocean waves in finite depth: unified
370 theory and application to radiation patterns, Geophys. J. Int., 21, 569-585, doi:10.1093/gji/ggaa015, 2020.

Donn, W. L., and Naini, B.: Sea wave origin of microbaroms and microseisms, J. Geophys. Res., 78, 4482-4488, doi:10.1029/JC078i021p04482, 1973.

Ceranna, L., Matoza, R., Hupe, P., Le Pichon, A. and Landès, M.: Systematic array processing of a decade of global IMS infrasound data, Infrasound monitoring for atmospheric studies, 2nd ed. Springer Nature, Dordrecht, ISBN: 978-3-319-75140-
375 5, 471–482, 2019.

Evers, L. G. and Haak, H. W.: Listening to sounds from an exploding meteor and oceanic waves, Geophys. Res. Lett., 28(1), 41–44, doi:10.1029/2000gl011859, 2001.

Evers, L. G. and Siegmund, P.: Infrasonic signature of the 2009 major sudden stratospheric warming, Geophys. Res. Lett., 36(23), doi:10.1029/2009gl041323, 2009.

380 Garcés, M.: On using ocean swells for continuous infrasonic measurements of winds and temperature in the lower, middle, and upper atmosphere, Geophys. Res. Lett., 31(19), doi:10.1029/2004gl020696, 2004.

Gutenberg, B.: Microseisms, microbaroms, storms, and waves in western North America, Eos Trans. AGU, 34(2), 161-173,

doi:10.1029/TR034i002p00161, 1953.

Hasselmann, K.: A statistical analysis of the generation of microseisms, Rev. Geophys., 1(2), 177, doi:10.1029/rg001i002p00177, 1963.

Hasselmann, K.: Feynman diagrams and interaction rules of wave-wave scattering processes, Rev. Geophys., 4(1), 1, doi:10.1029/rg004i001p00001, 1966.

Haubrich, R. A. and McCamy, K.: Microseisms: Coastal and pelagic sources, Rev. Geophys., 7(3), 539, doi:10.1029/rg007i003p00539, 1969.

Hupe, P., Ceranna, L., Pilger, C., De Carlo, M., Le Pichon, A., Kaifler, B. and Rapp, M.: Assessing middle atmosphere weather models using infrasound detections from microbaroms, Geophys. J. Int., 216(3), 1761–1767, doi:10.1093/gji/ggy520, 2018.

IFREMER: Wave Watch 3, [online] Available from: ftp://ftp.ifremer.fr/ifremer/ww3/ (Accessed 3 October 2018), 2018.

Kanamori, H. and Given, J. W.: Use of long-period surface waves for rapid determination of earthquake-source parameters, Phys. Earth Planet. Inter., 27(1), 8–31, doi:10.1016/0031-9201(81)90083-2, 1981.

Kedar, S., Longuet-Higgins, M., Webb, F., Graham, N., Clayton, R. and Jones, C.: The origin of deep ocean microseisms in the North Atlantic Ocean, Proc. R. Soc. A Math. Phys. Eng. Sci., 464(2091), 777–793, doi:10.1098/rspa.2007.0277, 2008.

KNDC: Observation network of the Institute of Geophysical Researches of the National Nuclear Center of the Republic of Kazakhstan., [online] Available from: http://www.kndc.kz/index.php?option=com_content&view=article&id=45&Itemid=147&lang=en (Accessed 3 October 2019), 2019.

Landès, M., Ceranna, L., Le Pichon, A. and Matoza, R. S.: Localization of microbarom sources using the IMS infrasound network, J. Geophys. Res. Atmos., 117(D6), n/a-n/a, doi:10.1029/2011jd016684, 2012.

Landès, M., Le Pichon, A., Shapiro, N. M., Hillers, G. and Campillo, M.: Explaining global patterns of microbarom observations with wave action models, Geophys. J. Int., 199(3), 1328–1337, doi:10.1093/gji/ggu324, 2014.

Longuet-Higgins, M. S.: A Theory of the origin of microseisms, Philos. Trans. R. Soc. A Math. Phys. Eng. Sci., 243(857), 1–35, doi:10.1098/rsta.1950.0012, 1950.

Matoza, R. S., Landès, M., Le Pichon, A., Ceranna, L. and Brown, D.: Coherent ambient infrasound recorded by the International Monitoring System, Geophys. Res. Lett., 40(2), 429–433, doi:10.1029/2012gl054329, 2013.

Olson, J. V and Szuberla, C. A. L.: Distribution of wave packet sizes in microbarom wave trains observed in Alaska, J. Acoust. Soc. Am., 117(3), 1032–1037, doi:10.1121/1.1854651, 2005.

Le Pichon, A., Ceranna, L. and Vergoz, J.: Incorporating numerical modeling into estimates of the detection capability of the IMS infrasound network, J. Geophys. Res. Atmos., 117(D5), n/a-n/a, doi:10.1029/2011jd016670, 2012.

Le Pichon, A., Assink, J. D., Heinrich, P., Blanc, E., Charlton-Perez, A., Lee, C. F., Keckhut, P., Hauchecorne, A., Rüfenacht, R., Kämpfer, N., Drob, D. P., Smets, P. S. M., Evers, L. G., Ceranna, L., Pilger, C., Ross, O. and Claud, C.: Comparison of co-located independent ground-based middle atmospheric wind and temperature measurements with numerical weather prediction models, J. Geophys. Res. Atmos., 120(16), 8318–8331, doi:10.1002/2015jd023273, 2015.Obrebski, M., F. Ardhuin,

F., E. Stutzmann, E., and M. Schimmel, M.: Detection of microseismic compressional (P)body waves aided by numerical modeling of oceanic noise sources,J. Geophys. Res. Solid Earth, 118, 4312–4324, doi:10.1002/jgrb.50233, 2013.

den Ouden, O., Assink, J. D., Smets, P., Shani-Kadmiel, S., Averbuch, G., and Evers, L.: CLEAN beamforming for the enhanced detection of multiple infrasonic sources, Geophys. J. Int, 221 (1), 305-317, doi:10.1093/gji/ggaa010, 2020.

Shapiro, N. M.: High-Resolution Surface-Wave Tomography from Ambient Seismic Noise, Science (80-.)., 307(5715), 1615–1618, doi:10.1126/science.1108339, 2005.

Shapiro, N. M. and Campillo, M.: Emergence of broadband Rayleigh waves from correlations of the ambient seismic noise, Geophys. Res. Lett., 31(7), doi:10.1029/2004gl019491, 2004.

Smets, P. S. M. and Evers, L. G.: The life cycle of a sudden stratospheric warming from infrasonic ambient noise observations, J. Geophys. Res. Atmos., 119(21), 12-84,99, doi:10.1002/2014jd021905, 2014.

Smirnov, A.: The variety Oof Infrasound sources recorded by Kazakhstani stations, in CTBT: Science and Technology, Vienna. [online] Available from: https://www.ctbto.org/fileadmin/user_upload/SnT2015/SnT2015_Posters/T2.3-P20.pdf, 2015.

Smirnov, A., Dubrovin, V., Evers, L. G. and Gibbons, S. J.: Explanation of the nature of coherent low-frequency signal sources recorded by the monitoring station network of the NNC RK, in CTBT: Science and Technology 2011. [online] Available from: https://www.ctbto.org/fileadmin/user_upload/SandT_2011/posters/T4-P12 A_Smirnov Explanation of the nature of coherent low-frequency signal sources recorded by the monitoring station.pdf, 2011.

Smirnov, A., De Carlo, M., Le Pichon, A. and Shapiro, N. M.: Signals from severe ocean storms in North Atlantic as it detected in Kazakhstan: observations and modelling, NNC RK Bull., (2), 152–160, 2018.

Smirnov, A., De Carlo, M., Le Pichon, A., Shapiro, N. and Kulichkov, S.: Results of the microseism and microbarom detections by the seismo-acoustic Kazakh network, doi:10.31905/dsw7l5bv, 2020.

Stehly, L., Campillo, M. and Shapiro, N. M.: A study of the seismic noise from its long-range correlation properties, J. Geophys. Res., 111(B10), doi:10.1029/2005jb004237, 2006.

Stutzmann, E., Ardhuin, F., Schimmel, M., Mangeney, A. and Patau, G.: Modelling long-term seismic noise in various environments, Geophys. J. Int., 191(2), 707–722, doi:10.1111/j.1365-246x.2012.05638.x, 2012.

Szuberla, C. A. L. and Olson, J. V: Uncertainties associated with parameter estimation in atmospheric infrasound arrays, J. Acoust. Soc. Am., 115(1), 253–258, doi:10.1121/1.1635407, 2004.

Toksöz MN, Lacoss RT. Microseisms: mode structure and sources. Science. 1968; 159 (3817): 872-873. doi:10.1126/science.159.3817.872

Waxler, R. and Gilbert, K. E.: The radiation of atmospheric microbaroms by ocean waves, J. Acoust. Soc. Am., 119(5), 2651–2664, doi:10.1121/1.2191607, 2006.

Waxler, R., Gilbert, K., Talmadge, C., and Hetzer, C.: The effects of finite depth of the ocean on microbarom signals, in 8th Int. Conf. Theoretical and Computational Acoustics (ICTCA), Crete, Greece, 2007.

Waxler, R., and Assink, J.: Propagation modeling through realistic atmosphere and benchmarking. In Infrasound monitoring

for atmospheric studies: 2nd ed. Springer Nature, Dordrecht, ISBN: 978-3-319-75140-5, 509-550, 2019.

Weaver, R. L. Information from seismic noise. Science, 307(5715), 1568-1569. https://doi.org/10.1126/science.1109834, 2005

455
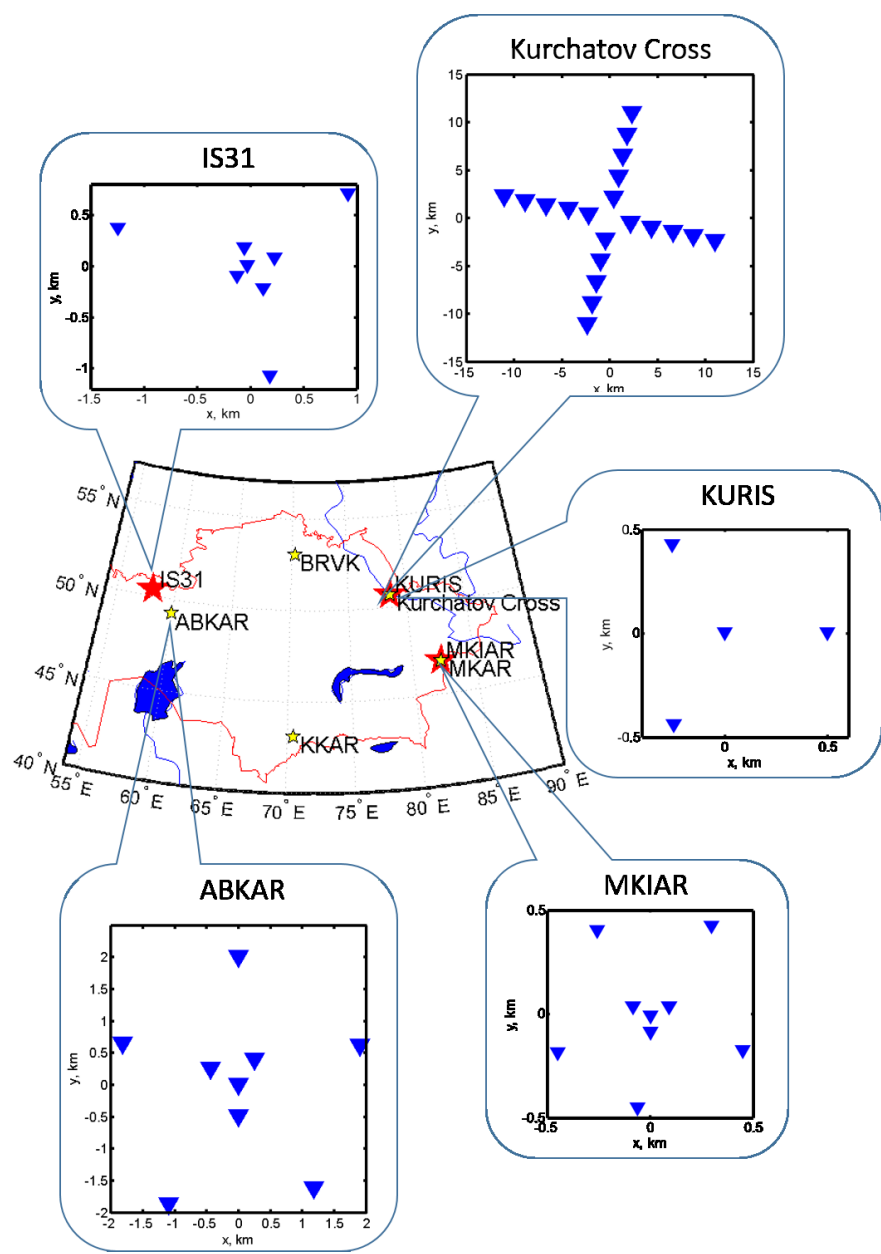
Figure 1. **IGR monitoring network. Yellow and red stars are seismic and infrasound arrays, respectively. Seismic and infrasound arrays are collocated at two sites. IS31 infrasound and ABKAR seismic arrays are located 200 km apart.**
460 **Callouts show the array configurations. the configurations are not shown for the KKAR and MKAR as they are similar to the ABKAR's one.**
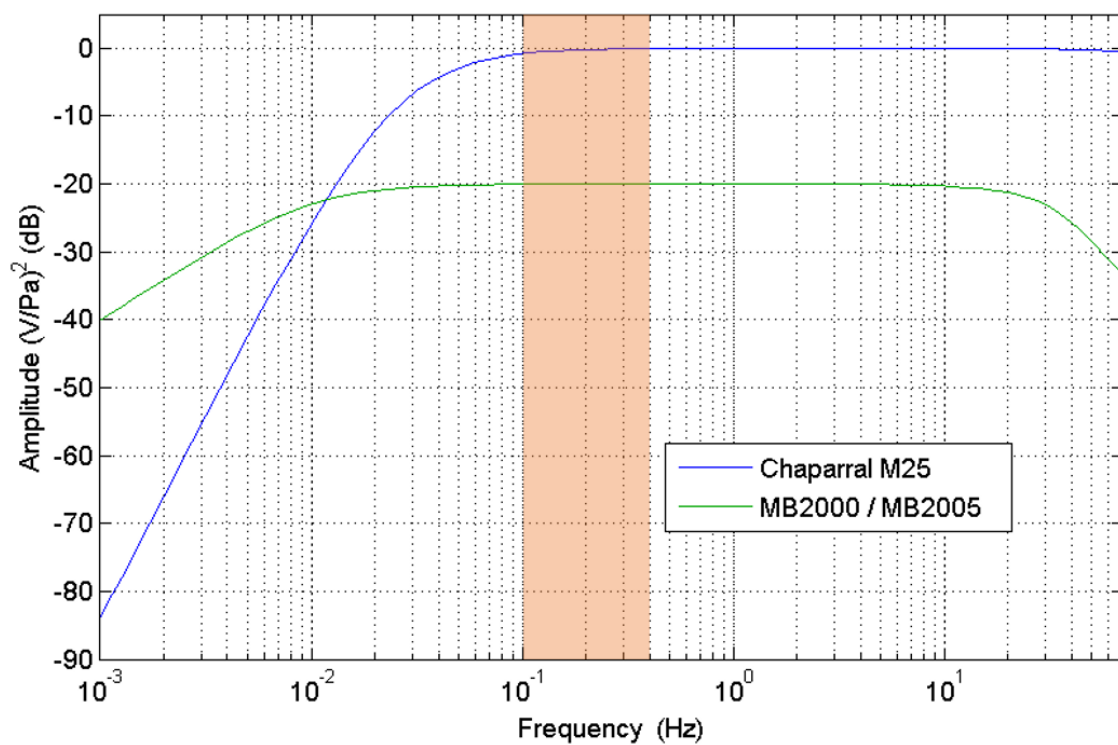
Figure 2.   **Frequency response of the MB2000, MB2005 and Chaparral M25 microbarometers.**
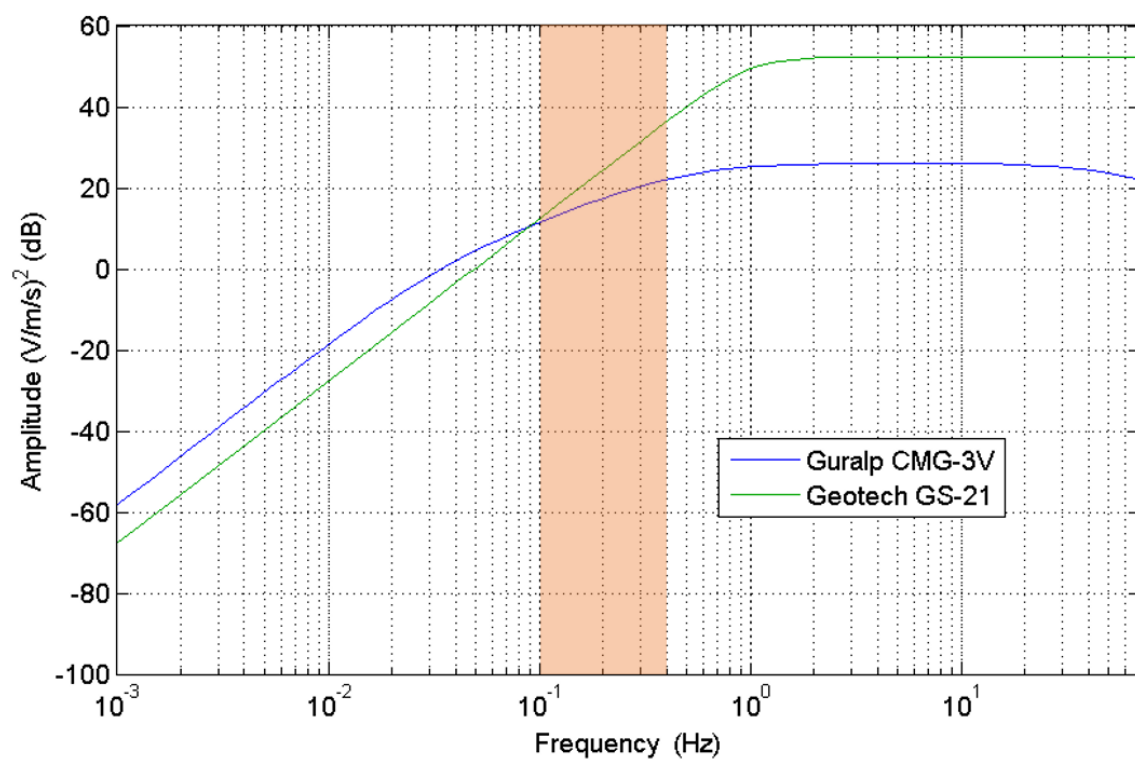
465

Figure 3. **Frequency responses of Geotech GS-21 Guralp CMG-3V seismometers**
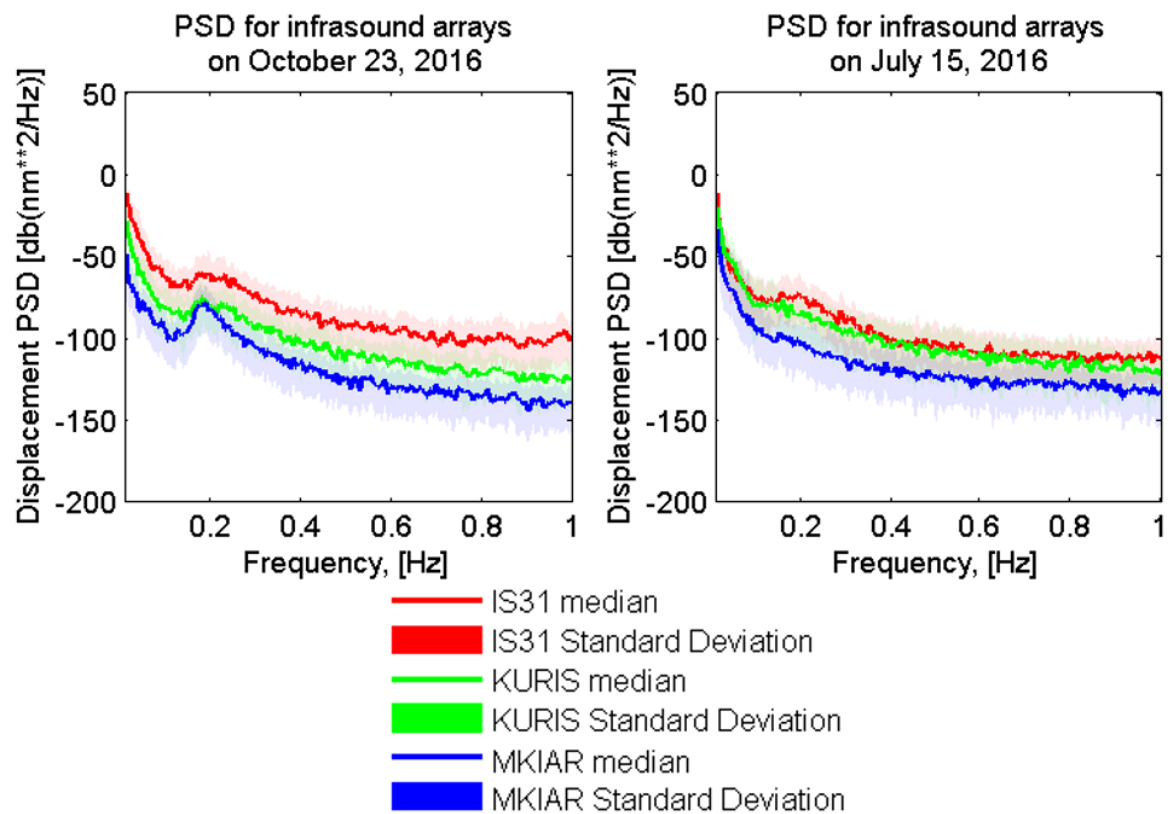
Figure 4.   **Noise spectra characteristics for the infrasound arrays.**

470
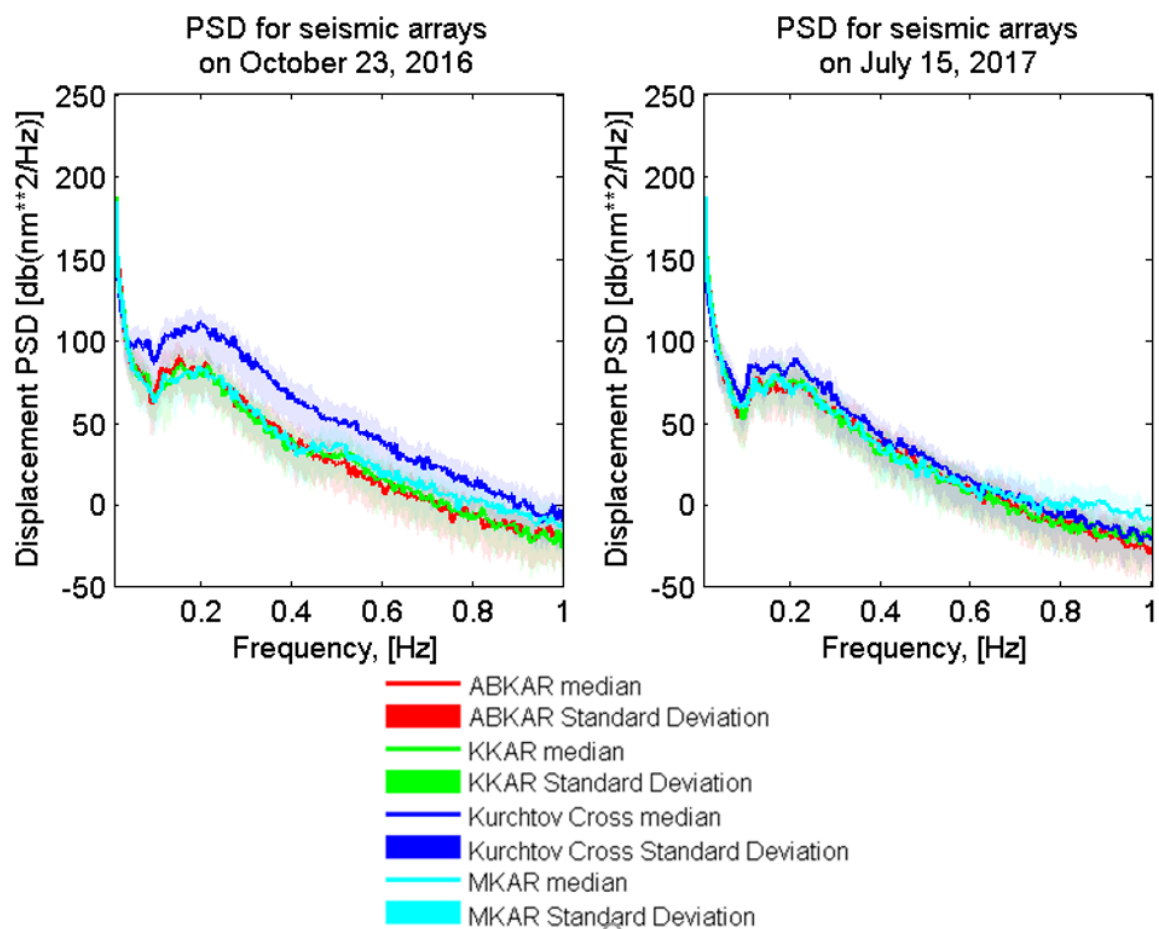
Figure 5. Noise spectra characteristics for the seismic arrays.
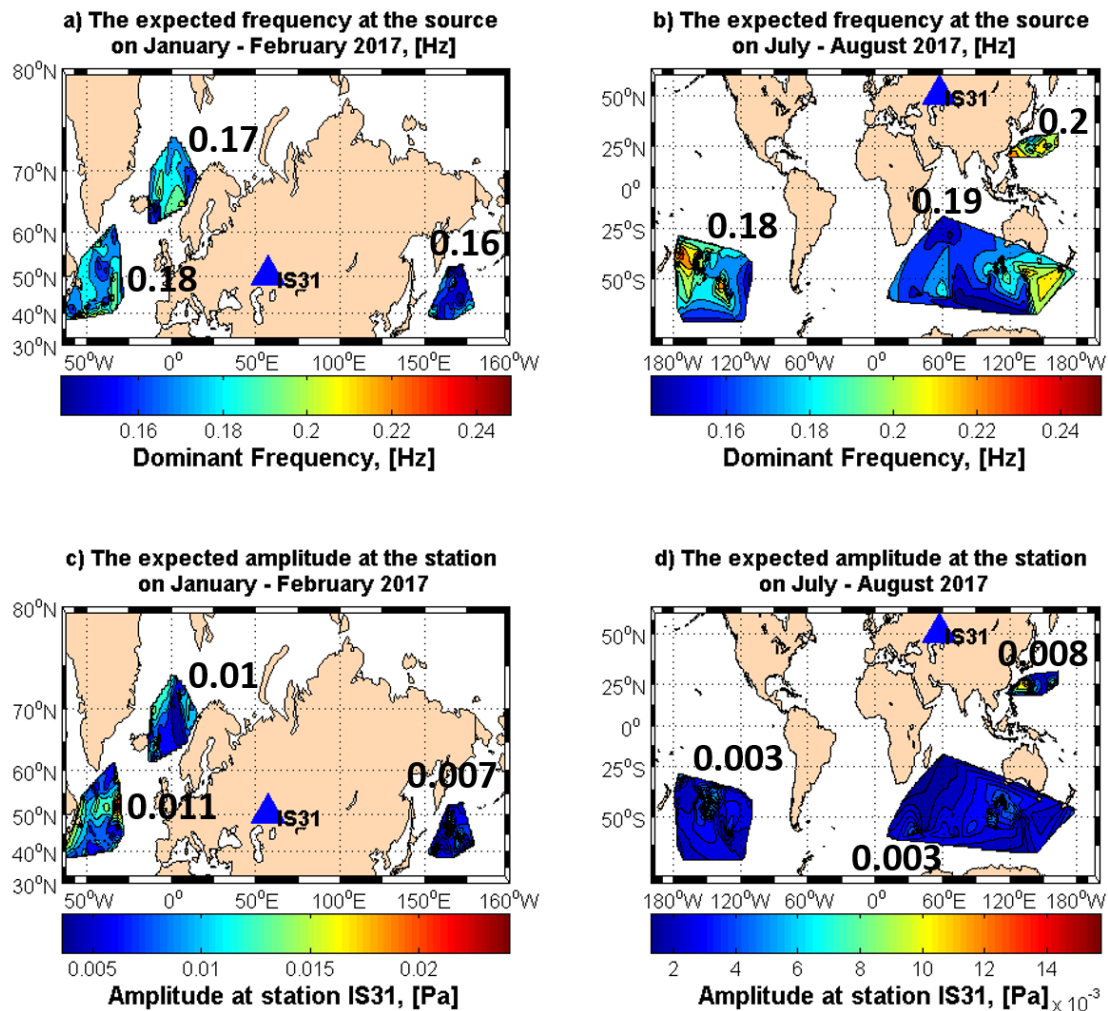
475

Figure 6. The distribution of the epicenters of the expected microbarom sources in January - February 2017 detected by the IS31 infrasound array.
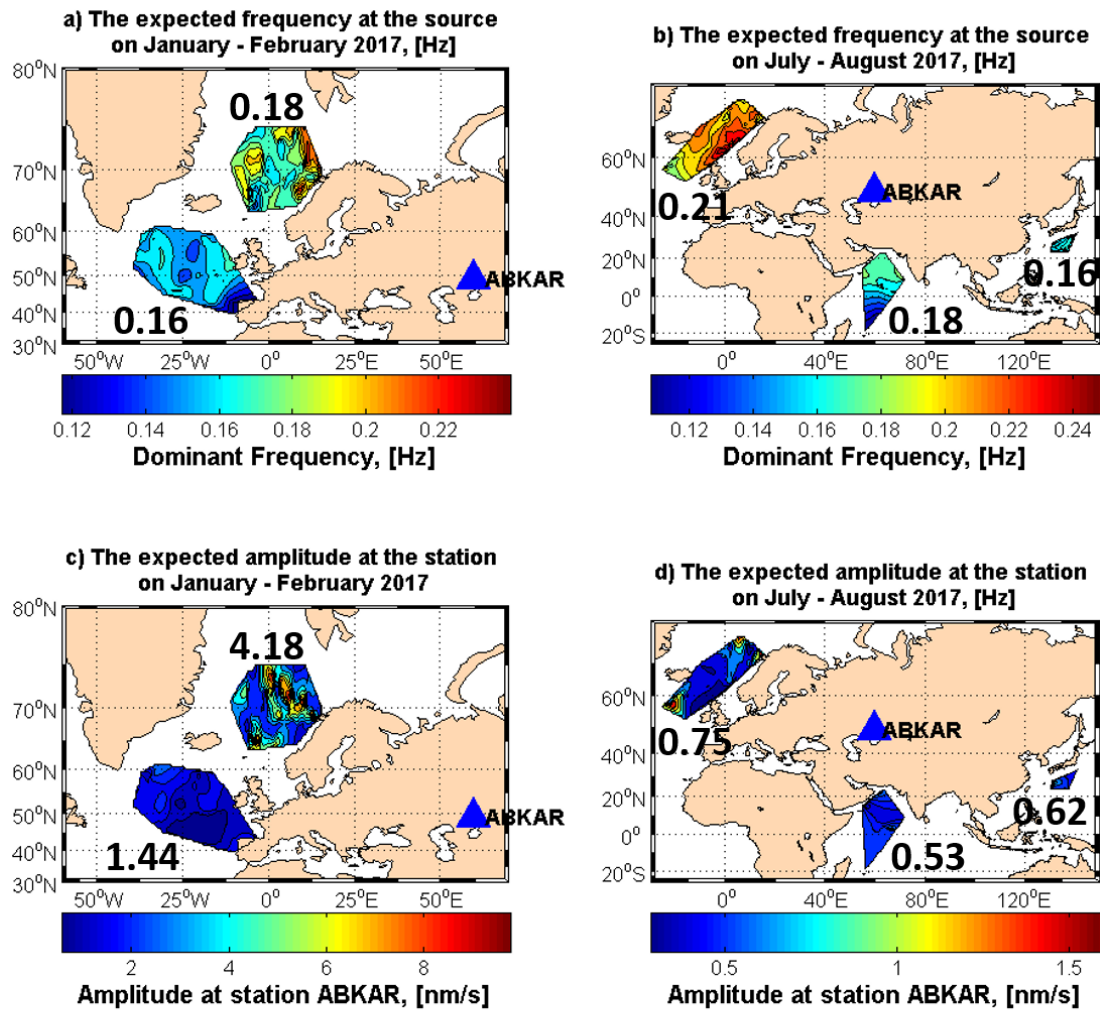
Figure 7. The distribution of the epicenters of the predicted microseism sources from January to February 2017 detected by the ABKAR seismic array.

485
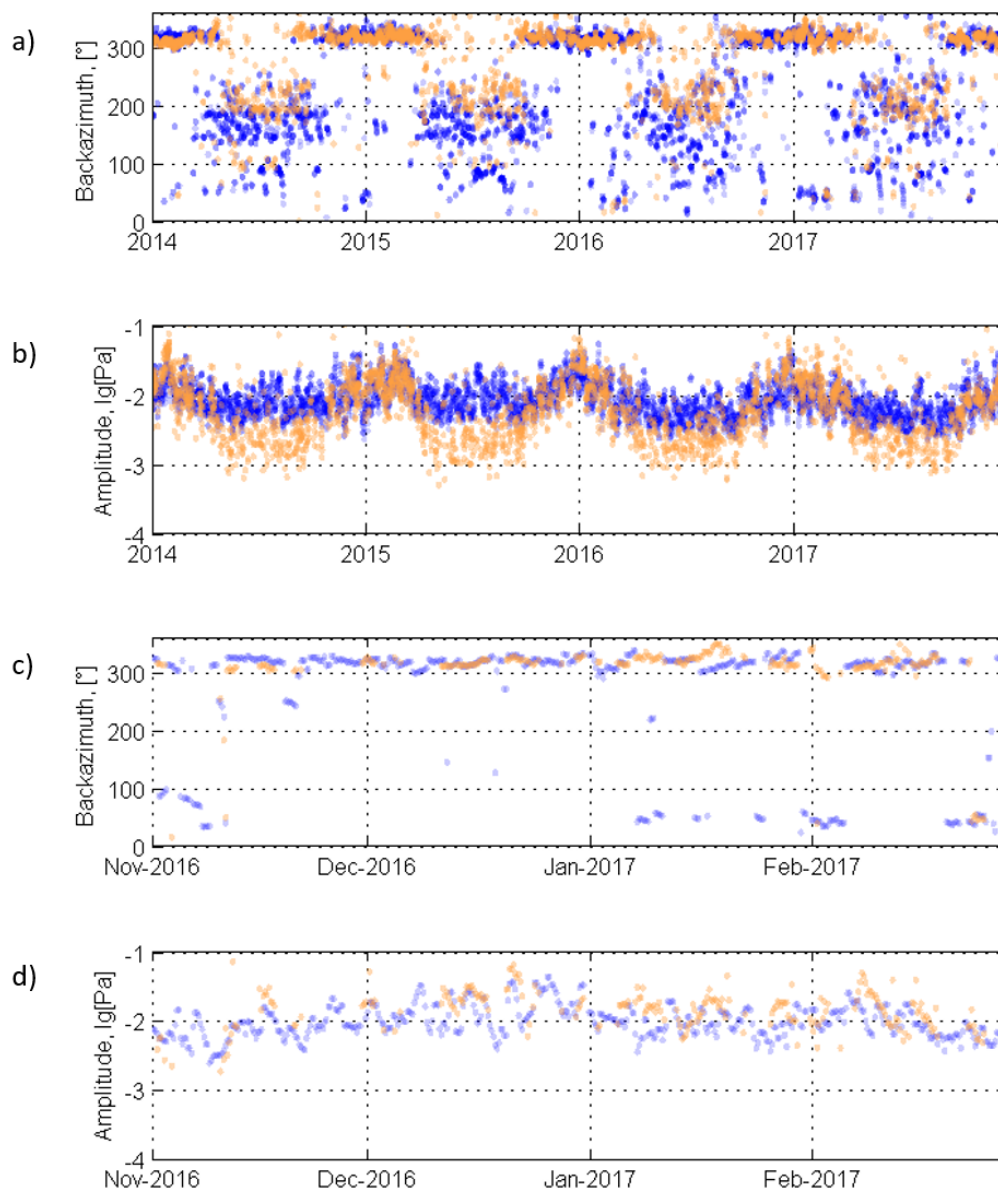
Figure 8. Dominant amplitude and back-azimuths of infrasound signals at IS31 with a time resolution of 6 hours from 1 January 1, 2014 to December 31, 2017 (orange circles). Blue circles denote simulated values. (c) and (d): detail from November 1, 2016 to February 28, 2017.
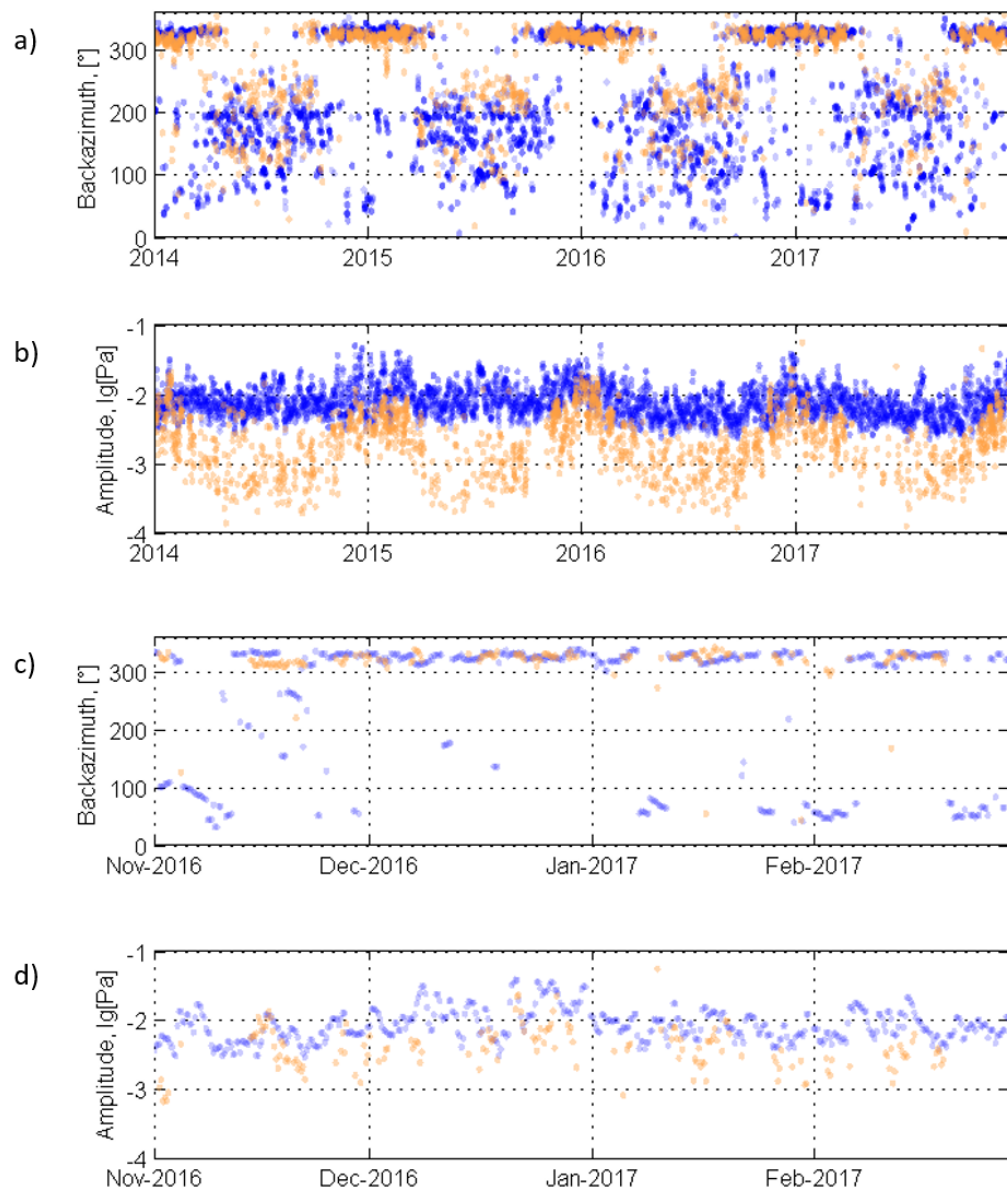
490

Figure 9.   **Same as Figure 8 at KURIS every from 1 January 1, 2014 to December 31, 2017.**
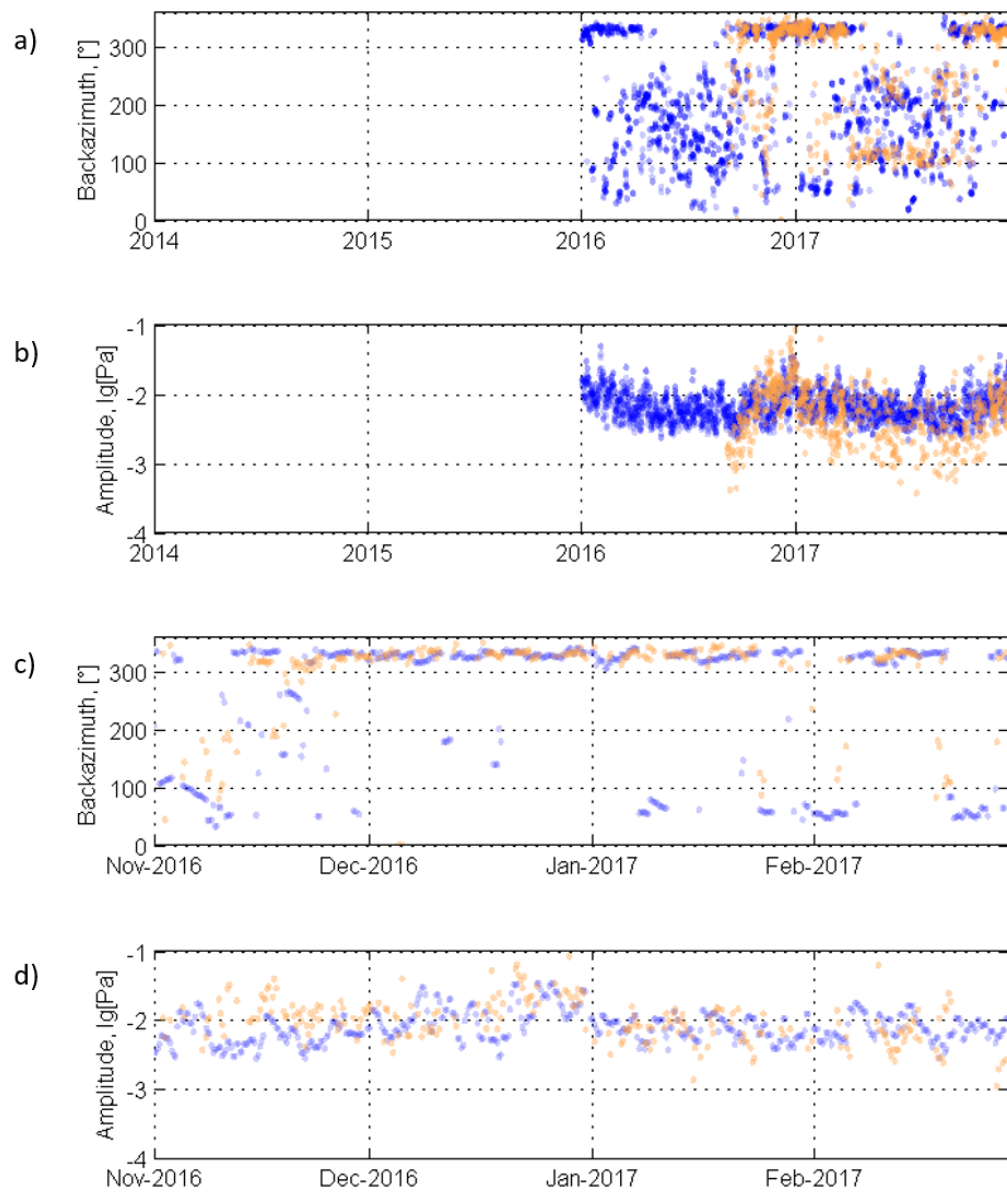
Figure 10. Same as Figure 8 at MKIAR from 1 January 1, 2014 to December 31, 2017.
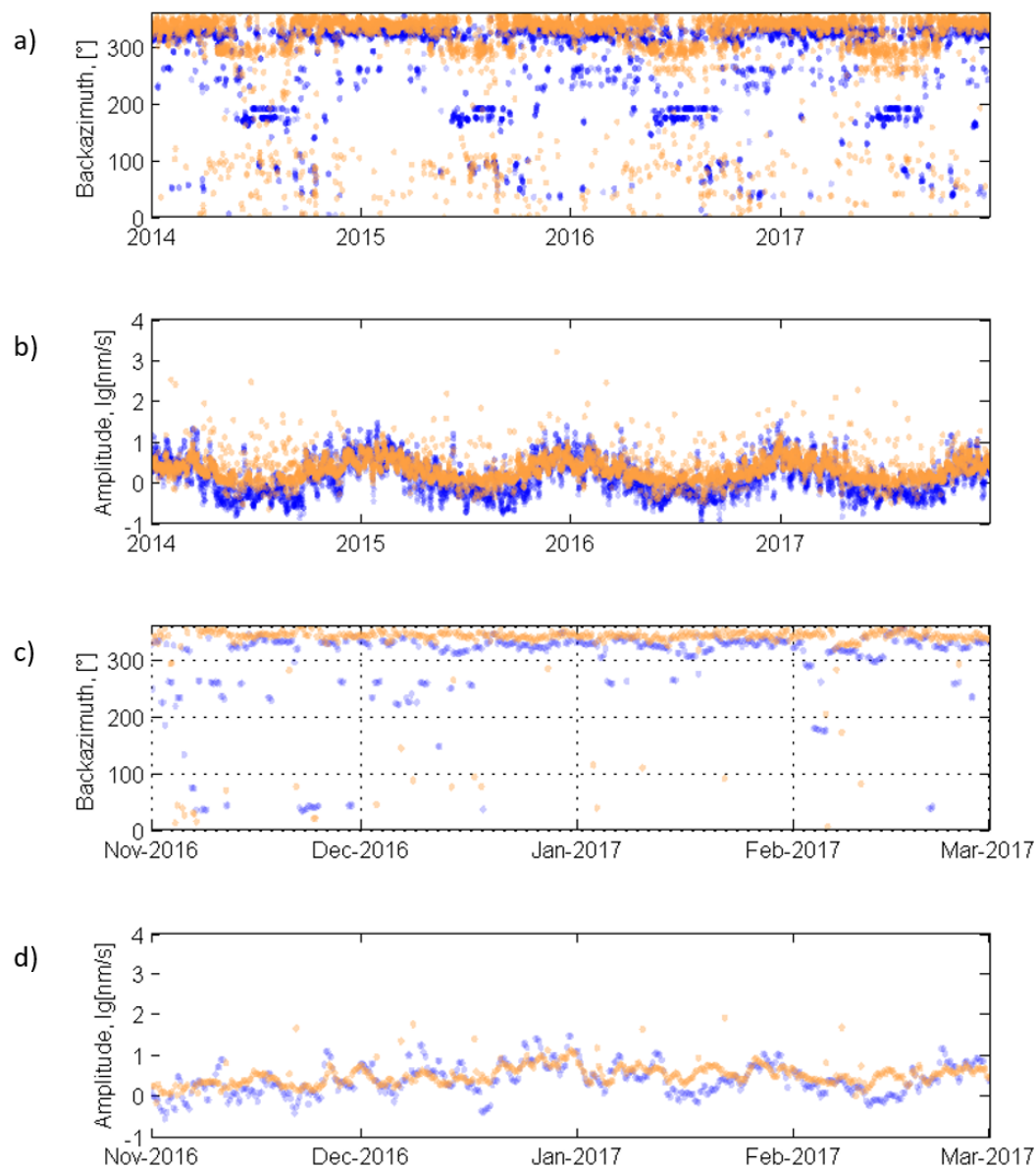
495

Figure 11. Same as Figure 8 at ABKAR from 1 January 1, 2014 to December 31, 2017.
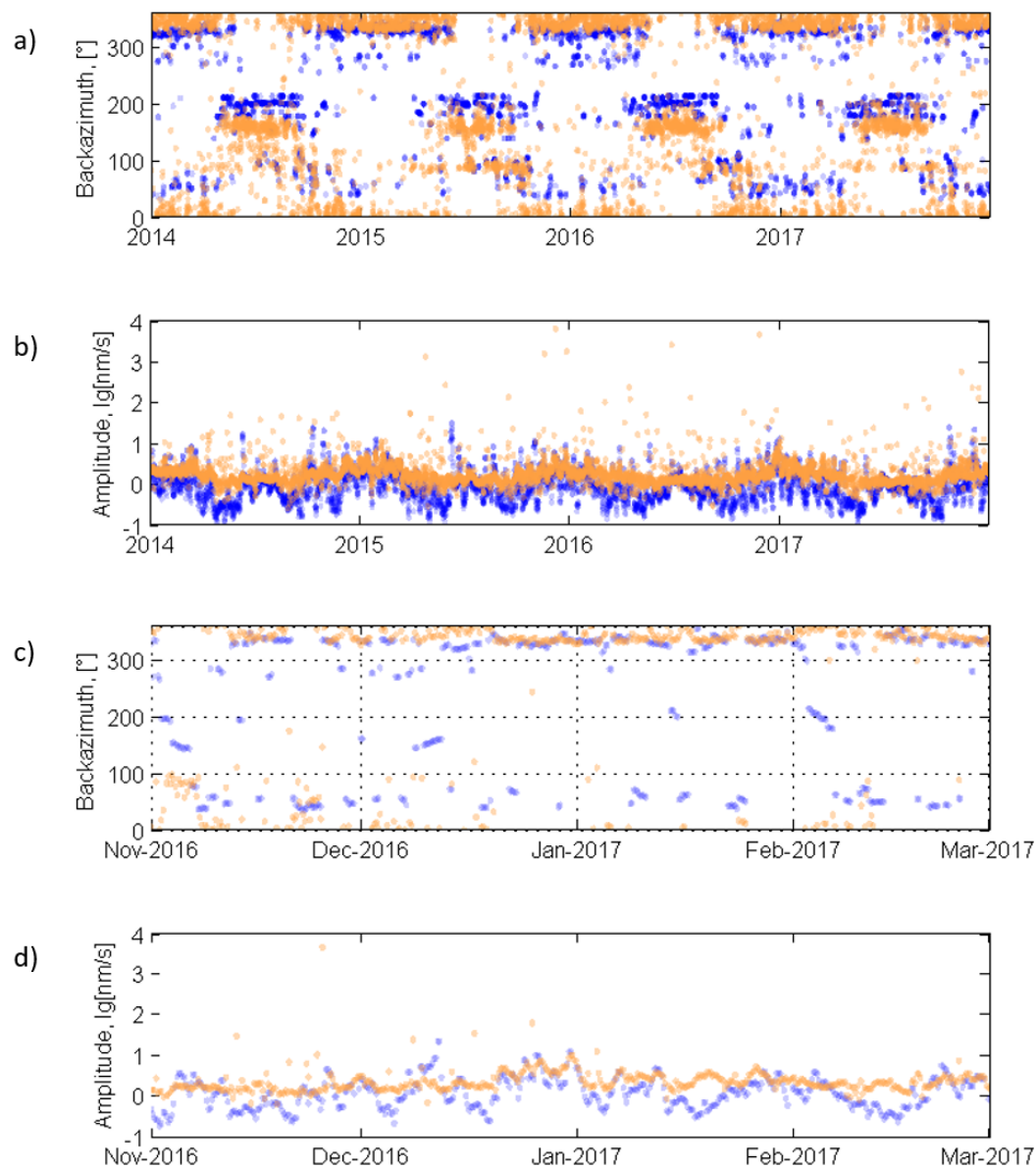
Figure 12. Same as Figure 8 at KKAR from 1 January 1, 2014 to December 31, 2017.
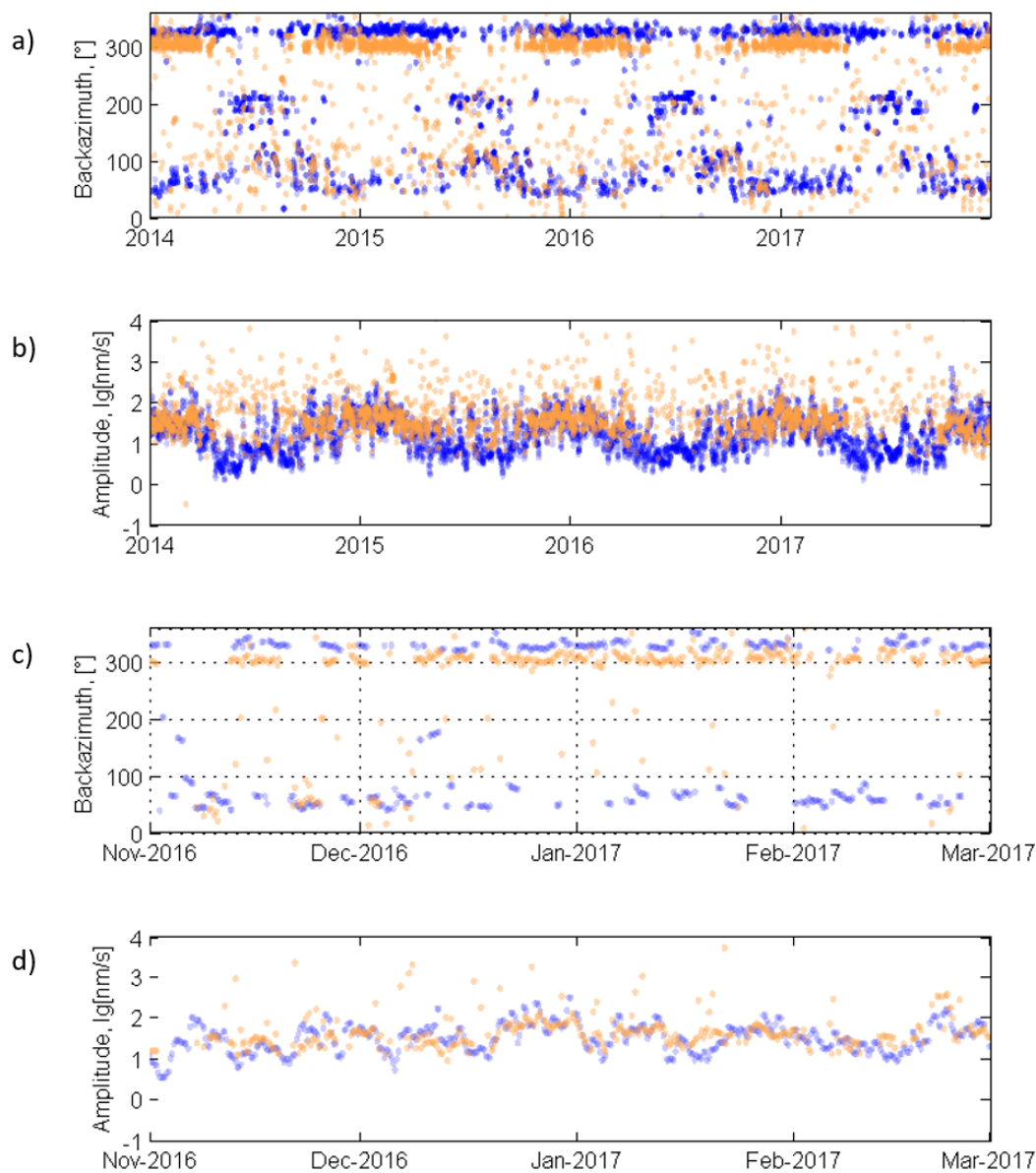
500

Figure 13. **Same as Figure 8 at Kurchatov Cross from 1 January 1, 2014 to December 31, 2017. Expected amplitudes are scaled to compensate the instrument response difference.**
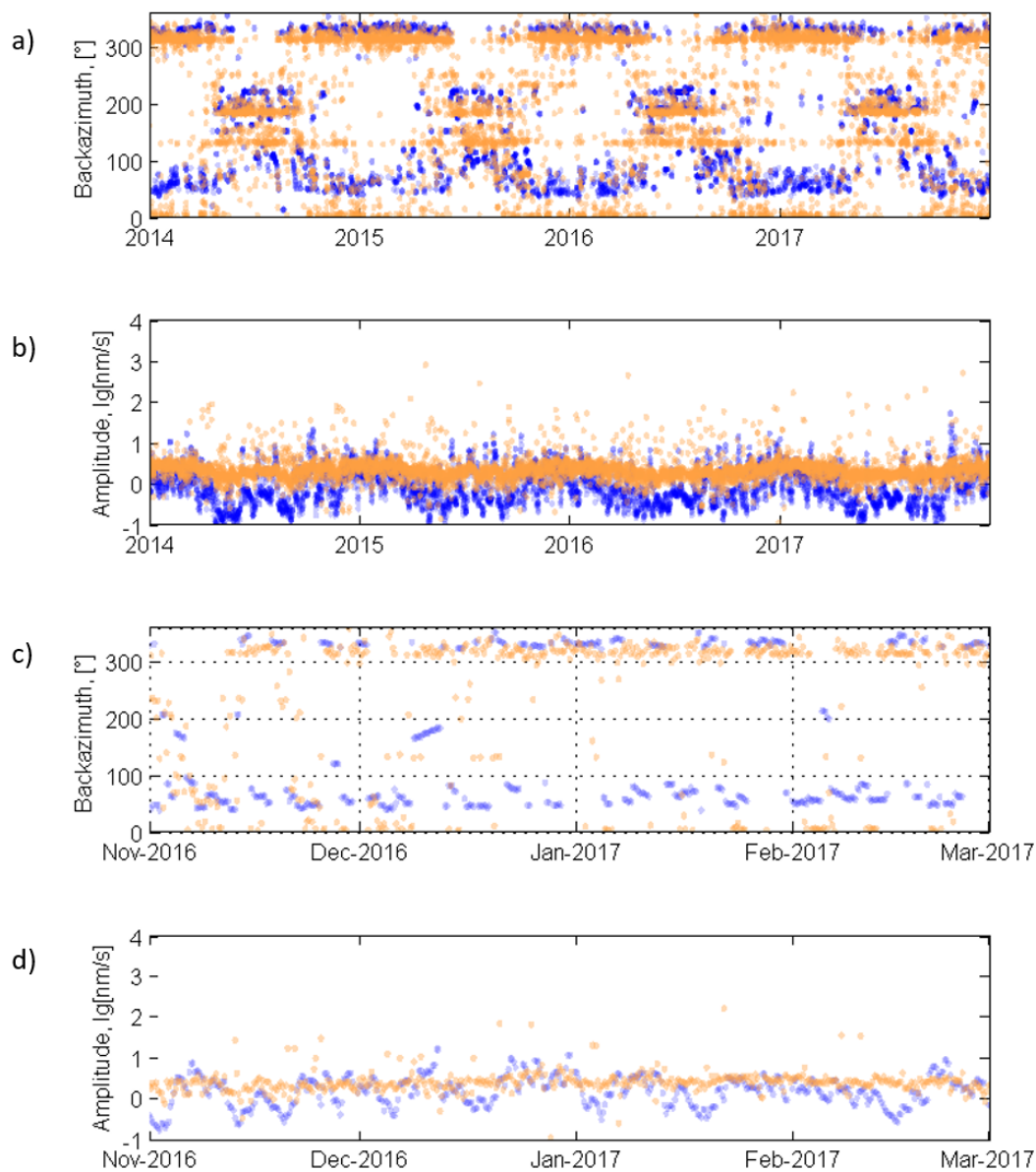
Figure 14.   **Same as Figure 8 at MKAR from 1 January 1, 2014 to December 31, 2017.**

505

a) Observations for the entire year 2017

b) Observations from December 1st 2016 to February 28th 2017

c) Observations from June 1st to August 31st 2017
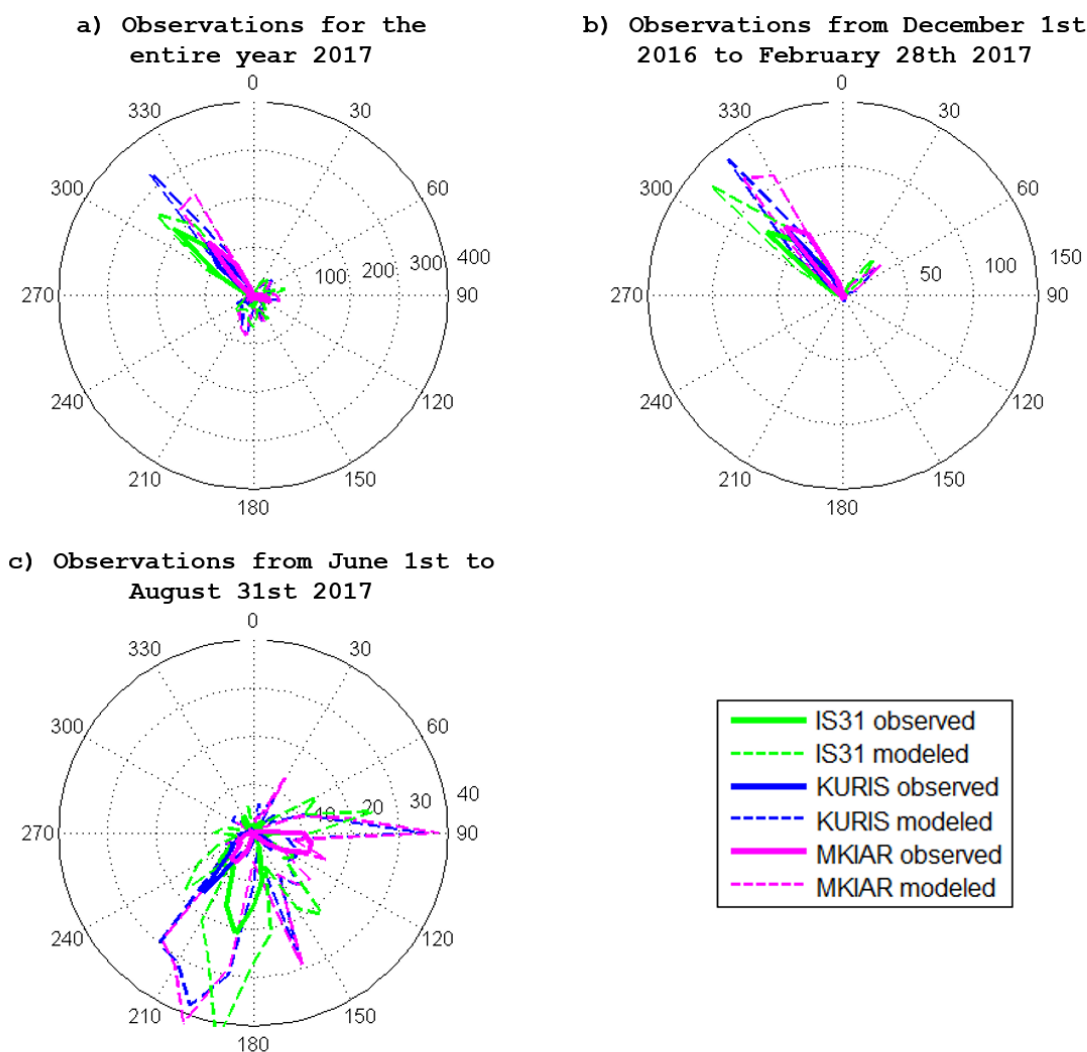
510

Figure 15. Azimuthal distribution of detections with maximum amplitudes for infrasound stations throughout 2017 (a), from December 1, 2016, to February 28, 2017 (b), and from June 1 to August 31, 2017 (c).
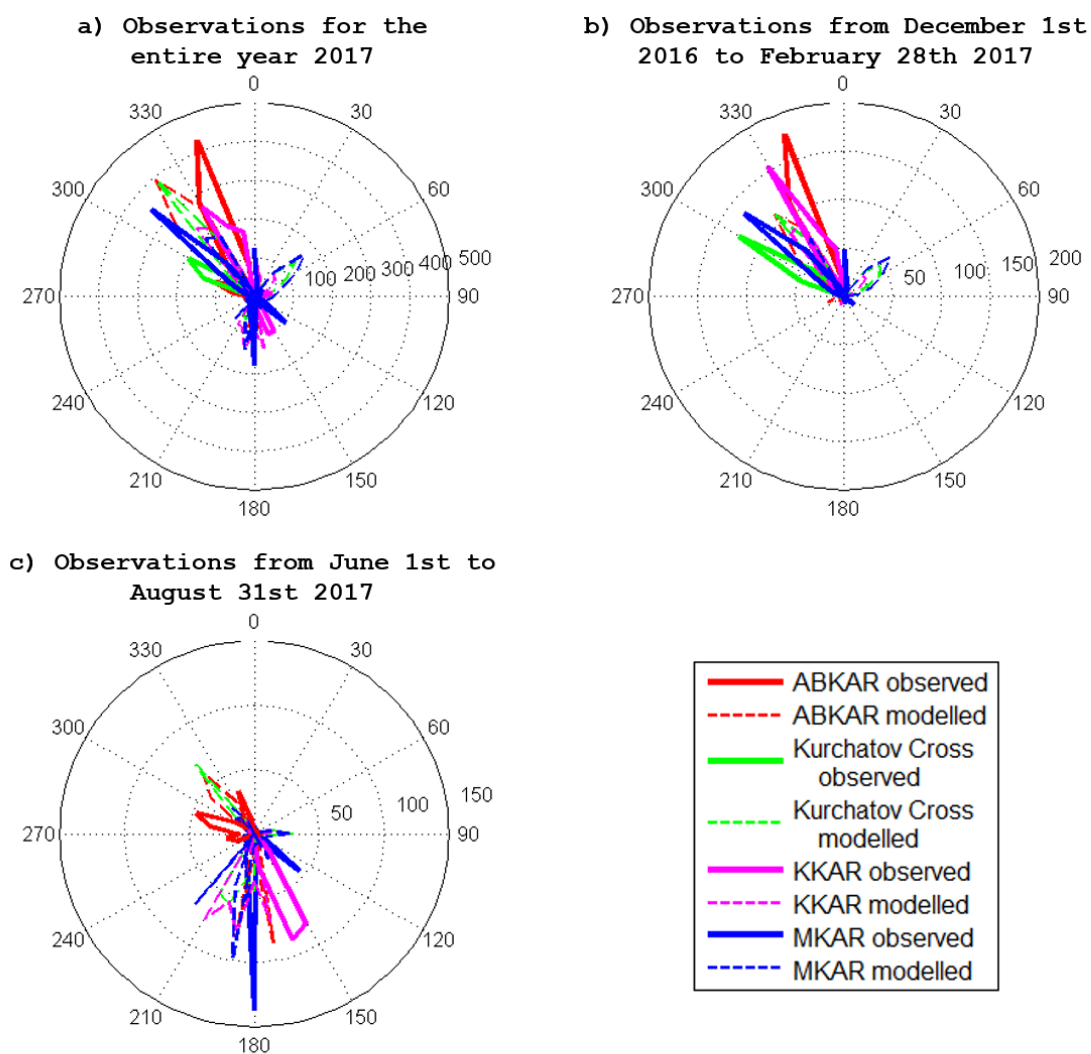
Figure 16. Azimuthal distribution of detections with maximum amplitudes for seismic stations throughout 2017 (a), from December 1, 2016, to February 28 (b), 2017, and from June 1 to August 31, 2017 (c).

515

520
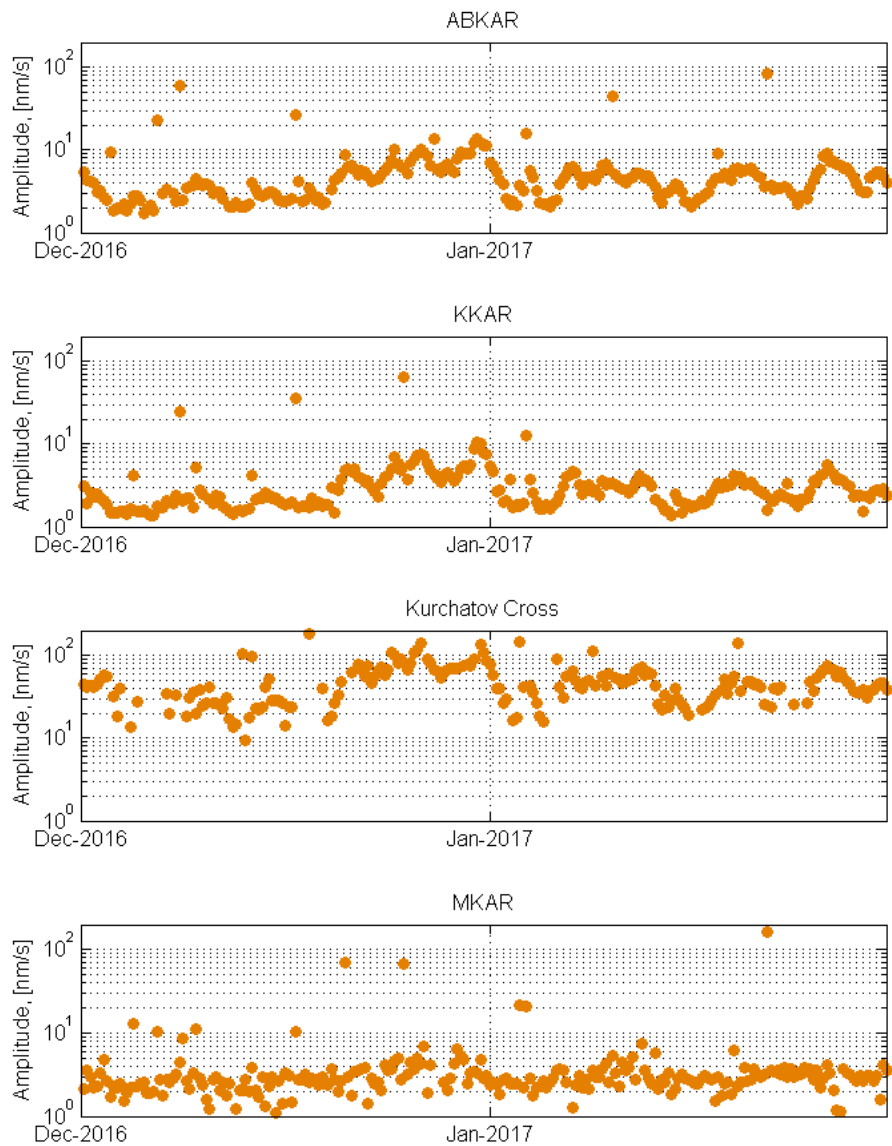
Figure 17. Dominant amplitude of seismic signals in the 0.1-0.4 Hz band detected at ABKAR (a), KKAR (b), Kurchatov Cross array (c), and MKAR (d) arrays from December 1, 2016 to January 31, 2017.
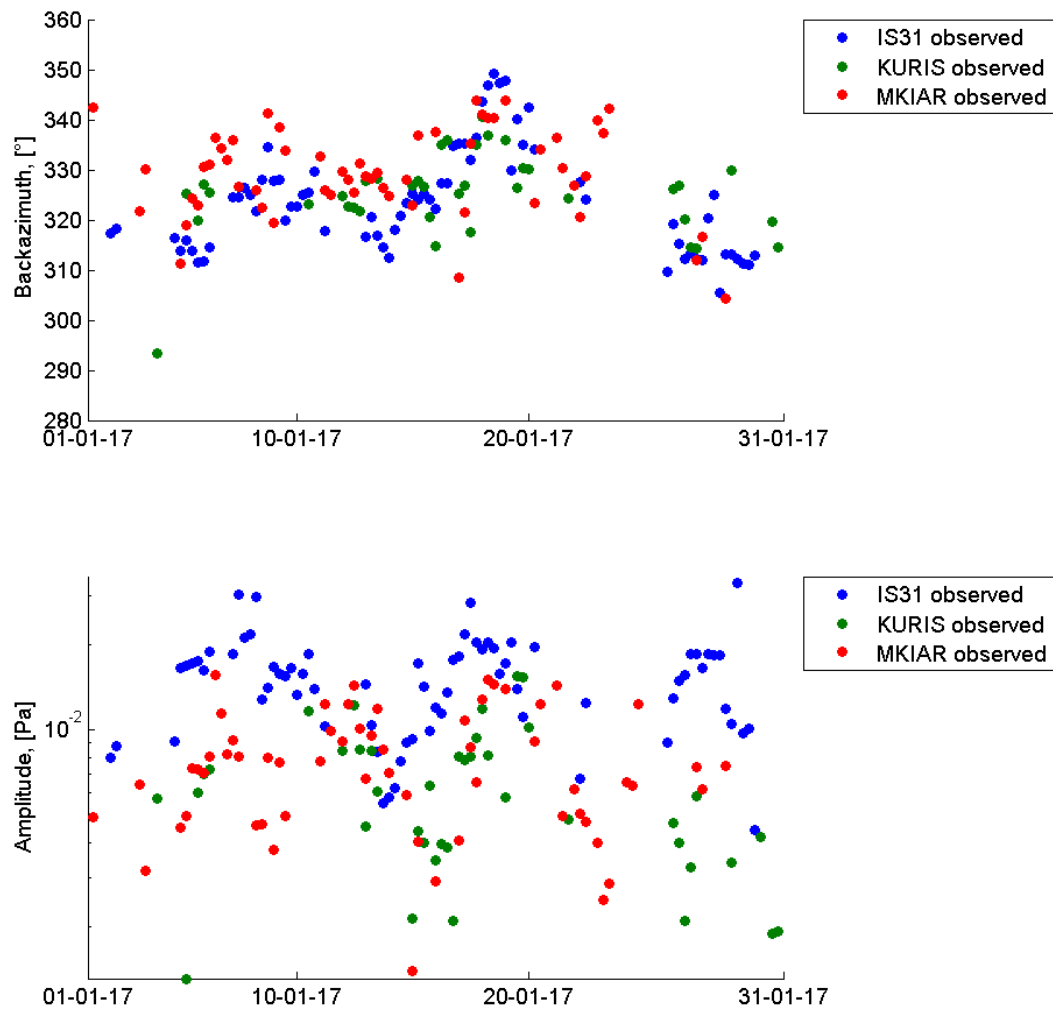
525   **Figure 18.**   **Spatio-temporal variations of microbarom parameters recorded at IS31, KURIS, and MKIAR. Back-azimuth (top) and amplitude (bottom) variations during January 2017.**
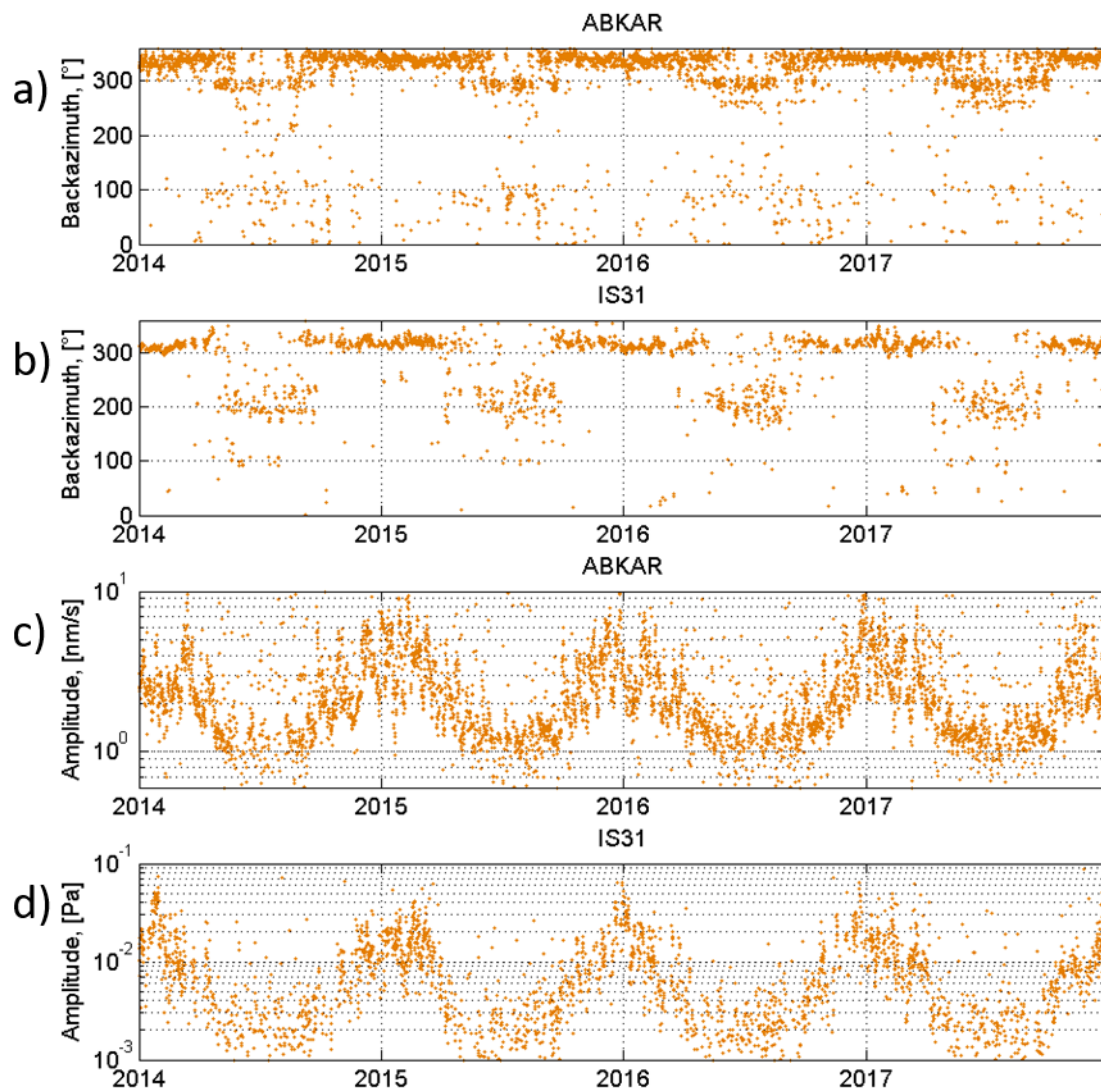
Figure 19. Comparison of the observation results at the ABKAR seismic array and IS31 infrasound station separated by 230 km.
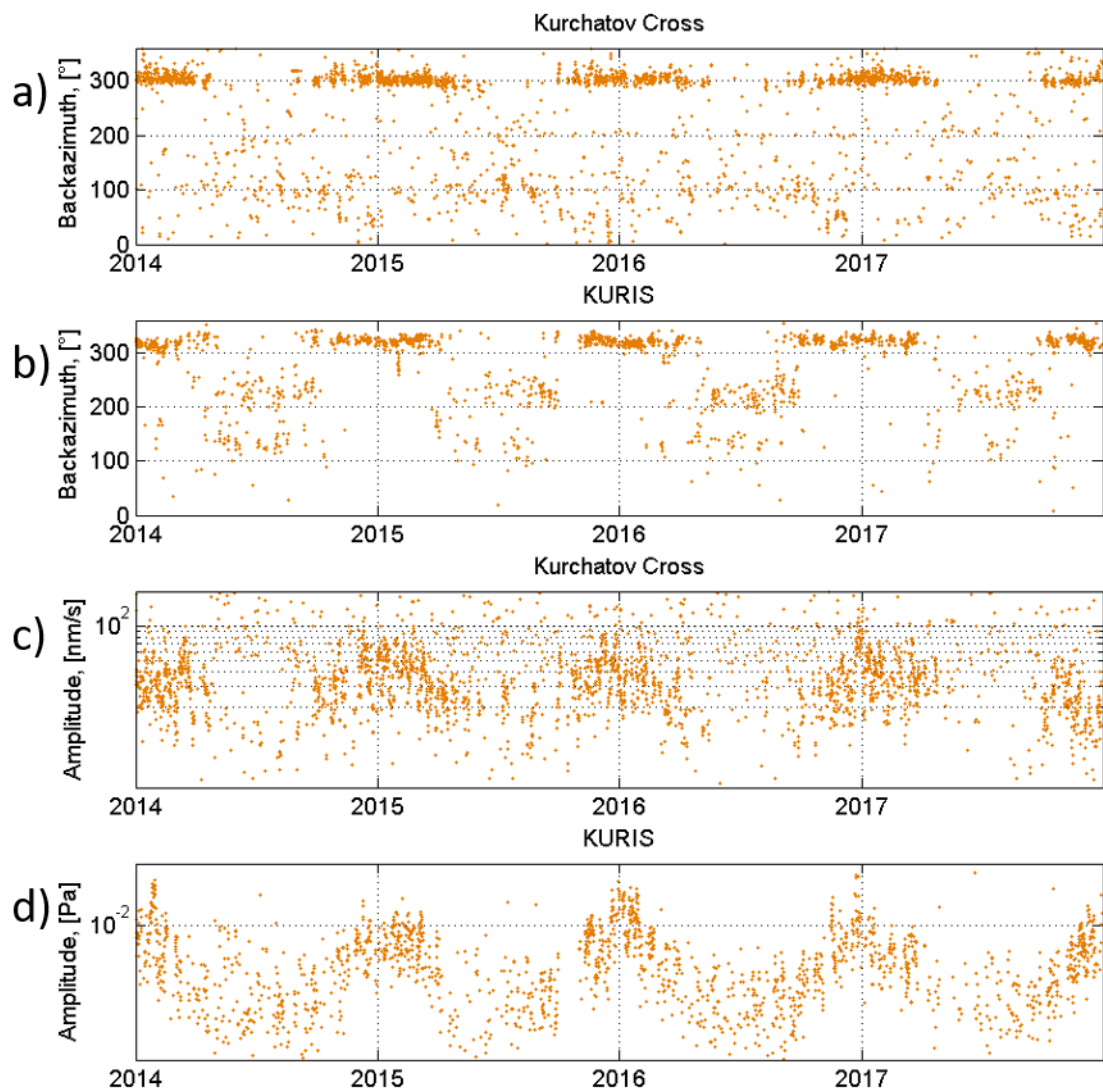
Figure 20. Comparison of the observation results at the collocated Kurchatov Cross seismic array and KURIS infrasound station.

Table 1. Uncertainties of azimuth and apparent velocity estimates.

Parameter	Horizontal velocity, m/s	IS31	KURIS	MKIAR	ABKAR	KKAR	MKAR	Kurchatov Cross

δΘ (°)	340	0.55 - 0.74	2.05 – 2.34	0.58 - 0.67			
δV (m/s)		3.8 – 4.4	12 - 14	3.5 – 3.9			
δΘ (°)	3000				4.89 – 5.64	5.14 – 6.30	4.55 – 6.84	0.48 – 0.49
δV (m/s)					250 – 290	270 – 330	220 - 380	25 – 26

Table 2. Estimations of the prediction quality for microbarom amplitudes and azimuths.

Station	Long-term Observation period	S_{corr_Az}	S_{corr_Amp}	Observation period on winter	S_{corr_Az}	S_{corr_Amp}	Observation period on summer	S_{corr_Az}	S_{corr_Amp}
IS31	2014 - 2017	0.61	0.39	Dec 2016 – Feb 2017	0.76	0.53	Jun 2017 – Aug 2017	0.44	0.26
KURIS	2014 - 2017	0.52	0.23	Dec 2016 – Feb 2017	0.82	0.58	Jun 2017 – Aug 2017	0.16	0.18
MKIAR	Sep 2016 – Dec 2017	0.62	0.5	Dec 2016 – Feb 2017	0.82	0.66	Jun 2017 – Aug 2017	0.34	0.39

540